Inhibition of therapy-resistant and metastatic melanoma by targeting the translation initiation complex

Yongmei Feng[1*], Ximena Diaz-Olea[1,2*], Mariia Radaeva[3], Mehdi Amiri[4], Hyunjeong Joo[2], Hyungsoo Kim[2], Xiurong Ke[2], Aniruddha J. Deshpande[1], Steven Olson[1], Predrag Jovanovic[5], Ian Pass[1], Qiyun Deng[4], Ikrame Lazar[6], Rabi Murad[1], Alfredo Molinolo[7], Eduard Sergienko[1], Jessie Villanueva[8], Ivan Topisirovic[5], Michael Jackson[1], Cristina Ferrone[2], Nahum Sonenberg[4], Artem Cherkasov[3], Ze'ev A. Ronai[2^]

[1]Cancer Center, Sanford Burnham Prebys Medical Discovery Institute, La Jolla, CA, 92037, [2]Jim and Eleanor Randall Department of Surgery and Department of Biomedical Sciences, Translational Research Institute, Cedars Sinai Medical Center, Los Angeles, CA, 90048, [3]Department of Urologic Sciences, University of British Columbia and Vancouver Prostate Center, Vancouver, BC V6H3Z6, Canada, [4]Department of Biochemistry, McGill University, Rosalind and Morris Goodman Cancer Institute, McGill University, Montreal, QC H3A 1A3, Canada, [5]Gerald Bronfman Department of Oncology, Department of Biochemistry, Division of Experimental Medicine for Translational Research, Lady Davis Institute for Medical Research, McGill University, Montreal, Quebec, H3T 1E2, Canada, [6]Centre De Biologie Intégrative, Unité MCD, CNRS- University of Toulouse, 31062 TOULOUSE, Cedex 09, FRANCE, [7]Department of Pathology, Univ. California San Diego, La Jolla, 92037, [8]Molecular Oncogenesis Program, Cancer Center, The Wistar Institute, Philadelphia, PA, 19104.

*Equal contribution

^Correspondence – Ze'ev Ronai, Department of Biomedical Sciences and Jim and Eleanor Randal Departament of Surgery, Translational Research Institute, Cedars Sinai Medical Center, 8700 Beverly Blvd. Los Angeles, CA, 90048, T- 310-423-4248, E – zeev.ronai@cshs.org

Keywords: eIF4F, translation initiation complex, melanoma, metastasis, HDAC inhibitors, autophagy inhibitors, DNA damaging drugs, doxorubicin.

Abstract

Elevated expression of components of the translation initiation complex (eIF4F) is frequent in cancer and results in enhanced synthesis of oncogenic proteins. Given its essentiality in normal tissues, targeting eIF4F is challenging. Here, combining chemical and in silico screens, we identified a small molecule (M19 and its analog M19-6) that targets the MA3 domain of the eIF4F subunit eIF4G1, interferes with eIF4F assembly and alleviates melanoma resistance to BRAF and MEK inhibitors. Ribosome profiling revealed that the M19-6 selectively perturbs the melanoma translatome, limiting synthesis of factors that promote cell proliferation and neoplastic growth. Screens in melanoma models revealed that M19-6 synergizes with autophagy or HDAC inhibitors in cell culture and potentiates anti-neoplastic and anti-metastatic effects of doxorubicin *in vivo*. Overall, we describe a novel eIF4F complex inhibitor that offers a new therapeutic modality to target clinically challenging melanomas and could provide a molecular basis for combination with currently employed therapies.

Introduction

Malignant melanoma is a rapidly metastasizing tumor that has served as a flagship model for cancer immunotherapy [1, 2], although challenged by emerging resistance, which limits therapy effectiveness [3, 4]. Among novel factors proposed to enhance immunotherapy or overcome drug resistance are components of the eIF4F complex [5-8]. However, a significant challenge in targeting the activity of eIF4F complex in tumors, is that this complex is essential for the viability of all cells.

Assembly of the eIF4F complex is the rate-limiting step in translation initiation [9]. Although eIF4F activity is required for cap-dependent translation of all cytoplasmic mRNAs, there is a notable difference in requirements for eIF4F by housekeeping mRNAs (which are efficiently translated even when eIF4F complex activity or levels are low) versus cancer-promoting mRNAs (which require high eIF4F levels for optimal translation) [10-12]. Accordingly, eIF4F activity is frequently higher in malignant than in normal cells [10, 13-16], providing a clinically exploitable therapeutic window [10, 13, 17, 18]. Elevated EIF4F levels, commonly seen in tumors, including melanoma [19, 20], correlate with poor prognosis [7, 19], and increased eIF4F activity is linked to mTORC1 hyperactivation and 4E-BP inactivation [14]. As the major eIF4G paralogue, eIF4G1 is frequently overexpressed in malignancies, where it reportedly contributes to tumorigenesis and cancer progression, in part by regulating the DNA damage response and cell cycle activity [14, 21-25].

Among small molecules that disrupt the eIF4F complex, we previously identified SBI-756, which binds to eIF4G1 and disrupts the eIF4F complex by targeting eIF4G1 independently of cellular 4E-BP status. This mechanism allows SBI-756 to act regardless of the eIF4E/4E-BP ratio in the cell [14]. Given that several oncogenes and tumor suppressors, including Myc and p53 [7, 26], converge on the eIF4F complex, targeting this complex holds a promise in overcoming challenges associated with tumor heterogeneity, metastasis, and drug resistance [7, 8, 21, 27]. eIF4F inhibitors currently being tested in preclinical studies and clinical trials include 4EGI-1, which binds to eIF4E and prevents its association with eIF4G in a 4E-BP-dependent manner; the eIF4A inhibitors hippuristanol and rocaglates (e.g., silvestrol); and cap analogs and mimetics that inhibit eIF4E binding to the 5' mRNA cap [7, 28, 29]. Among the more recently developed eIF4F complex inhibitors is eFT226 (zotatifin), which inhibits eIF4A activity [30] and has demonstrated effectiveness against *Kras*-mutant lung cancer cells and triple-negative breast cancer [31, 32]. eFT226 has now reached clinical evaluation. Finally, a second-generation, more potent eIF4A inhibitor, MG-002, has recently been developed [33].

We recently demonstrated that SBI-756 inhibits melanomagenesis in several mouse models of human and mouse cell xenografts, including the genetic *Nras*^{Q61K}*::Ink4a*$^{-/-}$ melanoma model

[34]. Independent studies have shown that SBI-756 is effective in a B-cell lymphoma model when combined with the BCL-2 inhibitor venetoclax [18]. Recent studies have revealed SBI-756's ability to promote anti-tumor immunity and attenuate the growth of pancreatic tumors in preclinical models [35]. SBI-756 treatment also promoted a gene expression signature resembling that caused by genetic ablation of eIF4G1 [21]. Analysis of genetic changes in melanoma cells resistant to SBI-756 identified several genes associated with the cell cycle and DNA repair, hallmarks of eIF4G1 inhibition [21]. Nonetheless, suboptimal biophysical properties of SBI-756 have limited its further development, prompting the creation of a new generation of eIF4G1 inhibitors.

Here, we identify the MA3 domain of eIF4G1 as the target of SBI-756 and categorize a new class of small molecules that directly target the MA3 domain. Among the selected small molecules, M19 and its analog M19-6, disrupt the eIF4F complex and interfere with eIF4A/eIF4G1 interaction. Ribo-seq analysis identified that M19-6 limited the translation of mRNAs implicated in cell cycle and translation processes. Remarkably, when used in conjunction with histone deacetylase or autophagy inhibitors, M19-6 effectively inhibited naïve and therapy-resistant melanoma in culture, whereas its combination with the DNA-damaging drug doxorubicin resulted in efficient inhibition of melanoma growth and metastasis in vivo. The nature of M19-6 provides a new therapeutic modality to reduce the growth and metastatic spread of melanoma.

Results

Identification of the eIF4G1 MA3 domain as an SBI-756 target.

To identify the eIF4G1 domain that binds SBI-756, we transduced the A375 and UACC903 human melanoma lines, both of which stably expressed Cas9 (see Methods for details), with an sgRNA library consisting of 947 guides to target the eIF4G1 gene. After selecting sgRNA-expressing cells, we treated them with increasing SBI-756 concentrations and then harvested viable cells for DNA extraction and sequencing to identify sgRNAs conferring SBI-756 resistance. That analysis identified two gRNAs targeting sequences either within (gRNA-235) or proximal to (gRNA-622) the eIF4G1 MA3 domain [36] (Figure 1a, Supplementary Figure 1a), suggesting that this domain is required for SBI-756 targeting. To verify that these sgRNAs conferred SBI-756 resistance, we transduced A375 melanoma cells with either gRNA-235 or gRNA-622 and selected individual clones that became relatively more resistant to SBI-756. One clone transduced with gRNA-235 exhibited a 14-base pair deletion within the MA3 domain, resulting in early termination of eIF4G1 mRNA and protein. In contrast, the clone transduced with gRNA-622 exhibited a 12-base pair deletion within a domain proximal to MA3, which did not promote early termination of eIF4G1 transcripts (Supplementary Figure 1b). Previous studies suggest that the MA3 domain is important for eIF4G1/eIF4A interaction [37-40]. These findings are

consistent with our analysis performed in *S. Cerevisiae* transduced with an eIF4F gene set library and aimed at identifying components of the translation initiation machinery that confer SBI-756 resistance. That search revealed that expression of truncated forms of eIF4G1 and eIF4A1 genes (TIF1) is sufficient to confer SBI-756 resistance (Supplementary Figure 1c).

We next assessed viability of single clones expressing either gRNA-235 or gRNA-622 after SBI-756 treatment. Compared to control (EV) sgRNA-transduced cells, melanoma cells expressing either gRNA-235 or gRNA-622 exhibited increased SBI-756 resistance (Figure 1b). gRNA-235-transduced melanoma cells also showed decreased proliferation relative to EV- or gRNA-622-transduced cells (Supplementary Figure 1d).

Since SBI-756 disrupts eIF4F complex assembly [8], we asked whether melanoma cells expressing either gRNA-235 or gRNA-622 show changes in eIF4F complex composition. Using pull-down analysis with the methyl-^{7}GTP cap analogue to capture complex components, we observed that eIF4F complex levels were lower in melanoma cells expressing gRNA-235, as indicated by a notable decrease in eIF4G1 and increased abundance of 4E-BP1 in pulled-down proteins, as compared to EV controls or gRNA-622-expressing cells (Figure 1c). Conversely, SBI-756 treatment disrupted eIF4F complex formation in EV cells, but not in gRNA-235-expressing cells._Interestingly, gRNA-622-expressing cells did not exhibit eIF4F complex dissociation and continued to respond to SBI-756 treatment, suggesting that a different mechanism underlies melanoma resistance to SBI-756 in this context. Given that the MA3 domain is implicated in eIF4A/eIF4G1 interaction, we asked whether this interaction was disrupted in melanoma cells expressing mutant eIF4G1 forms. While melanoma cells expressing gRNA-235 showed clearly disrupted eIF4A/eIF4G1 interaction, based on IP analysis, that interaction was unchanged in gRNA-622-expressing cells (Figure 1d),_again suggesting that distinct mechanisms mediate effects of gRNA-235 and gRNA-622 on melanoma cell resistance to SBI-756.

To characterize possible differences in translation activity between MA3-mutant and control cells, we performed polysome profiling [41, 42] of single-cell clones harboring the MA3 mutation within eIF4G1. Notably, heavy polysome-to-monosome ratios seen in MA3-mutant melanoma cells and SBI-756-treated parental cells largely overlapped (Figure 1e). Moreover, relative to vehicle controls, SBI-756 treatment dramatically decreased the heavy polysome-to-monosome ratio in parental but not gRNA-235- or gRNA-622-expressing melanoma cells (Figure 1e). These observations suggest that MA3 mutations generated in our CRISPR screen likely perturb SBI-756 effects on the eIF4F complex.

An in silico screen identifies small molecules binding to the MA3 domain.

To identify small-molecule inhibitors of MA3 domain, we conducted an *in silico* screen based on the human eIF4GI crystal structure (PDB:1UG3) of a surface binding site in the protein's C-terminus [43]. That site included amino acid residues Ala1292, Ile1293, Glu1343, Thr1346,

Gln1350, Leu1384, and Lys1386 within the MA3 domain, which is predicted to be essential for drug binding. This selection was informed by blind docking experiments with SBI-756 and assessment of druggability of the MA3 domain surface. Molecular dynamics simulation (30ns, using the Desmond suite from Schrodinger; [44]) also revealed that SBI-756 formed stable interactions with these residues (Figure 2a). Druggability of the selected pocket was strongly suggested by both the depth and hydrophobic characteristics of the binding cavity and stability of these interactions (Figure 2a).

Next, to identify small-molecule eIF4G1 inhibitors, we performed virtual screening of the MA3 binding pocket by screening a library of 10 million drug-like compounds through molecular docking followed by filtering steps [45]. The initial docking phase identified 54,500 compounds exhibiting more favorable docking scores than the benchmark compound SBI-756. From this pool, we selected a chemically diverse subset of 500 compounds using filtration tools described in the Methods section. Final selection was carried out to exclude compounds with undesirable properties such as toxicity, promiscuity, and low solubility, resulting in 150 compounds, which were then clustered based on chemical diversity to yield 67 potential MA3 domain inhibitors (Supplementary Figure 2a).

Assessment of lead MA3-interacting compounds in melanoma.

Among the 67 potential MA3 protein inhibitors described above, 63 were available and purchased from ChemBridge (CB), Enamine (E), and Molport (M). We assessed all 63 for (i) toxicity to melanoma and other tumor lines, (ii) effect on melanoma lines relative to non-transformed melanocytes, and (iii) impact on gRNA-235-transduced melanoma cell lines. Initially, we tested compounds for toxicity against six melanoma lines representing diverse genetic mutations, as well as a prostate cancer and a pancreatic cancer line. Of the 63 compounds evaluated, 4 (CB6, E8, E10, and M19) were selected for further analyses (Supplementary Figure 2b), and, among them, E10 and M19 exhibited selectivity for melanoma cells relative to the immortalized melanocyte line H3A (Figure 2b). Relative to EV-transduced controls, compound M19 was less toxic to A375 cells expressing gRNA-235 (Supplementary Figure 2c). Decreasing serum levels further sensitized A375 melanoma cells to M19 treatment (Supplementary Figure 2d). Finally, among selected compounds, M19 was the most potent in disrupting both eIF4G1:eIF4A binding and eIF4F complex assembly (Figures 2c, 2d). Collectively, these data led us to select M19 for further experimental validation.

M19 treatment of melanoma cells perturbs gene expression.

To identify possible changes in gene expression following M19 treatment, we performed RNA-Seq using A375 melanoma cells treated 24 hours with either vehicle control or M19 compound (20 μM). Differential expression analysis identified 633 genes upregulated and 543 downregulated following M19 treatment (Figure 3a). Gene set enrichment analysis (GSEA) of these genes showed enrichment of pathways involved in apoptosis, the UPR, ROS signaling, and mTORC1 and p53 signaling (Supplementary Figure 3a). These pathways may underlie the toxicity that we observed in cultured tumor cells after M19 treatment and are consistent with pathways altered by inhibition of translation initiation complex components [21]. Ingenuity pathway analysis (IPA) of these gene sets further identified activation of oxidative stress response pathway genes associated with NRF2 as well as UPR and WNT/beta-catenin signaling pathway genes (Supplementary Figure 3b, Supplementary Table 1). Quantitative PCR of 14 upregulated and 2 downregulated genes confirmed these expression changes (Supplementary Figure 3c). Among downregulated pathways were E2F target genes and genes involved in the G2M cell cycle control, changes confirmed by qPCR analysis (Supplementary Figure 3d).

Characterization of select M19 analogs.

We next initiated a similarity search using the M19 scaffold as the basis to identify analogs with potentially greater efficacy. To do so, we screened the entire ZINC20 library, retrieving 3000 compounds with a Tanimoto similarity score above 0.65. Compounds with undesirable characteristics were eliminated using the same filtration process used in the initial structure-based screen. We then compared docking scores of analogs against the parental compound M19 to identify those with superior scores. Through a rigorous selection process (see methods for details), we identified and subsequently acquired 13 M19 analogs, all predicted to have enhanced binding affinity to the MA3 domain.

Further evaluation of 13 M19 analogs revealed that four (M19-5, M19-6, M19-12, and M19-13) demonstrated enhanced potency relative to M19 itself, based on analysis in A375 cells (Supplementary Figure 4a). Of these, M19-6 was the most potent compound in both colony-forming (CFE, Supplementary Figure 4b) and spheroid formation (Figure 3b) assays. M19-6 was also superior in promoting eIF4F complex dissociation compared to M19 (Figure 3c). Thus, we selected M19-6 for further characterization, given its greater potency against melanoma relative to melanocytes and based on gene expression changes seen in treated cells. These changes reflected those seen after M19 treatment, the most notable being in UPR (ATF4, DDIT3, and ATF3) and ROS (ERN1, HERPUD1, HHMOX, and c-Jun) signaling (Supplementary Figure 4c). Moreover, analysis of mRNA translation in the presence of M19-6 or other protein synthesis inhibitors revealed dose-dependent inhibition by M19-6. In this assay, M19-6 was more potent than the commercial inhibitor 4EGI-1, which blocks eIF4E-eIF4G1 binding and is known to be

toxic (Supplementary Figure 4d). Treatment with high M19-6 concentrations effectively induced A375 melanoma cell death, even following washes to remove the drug from the medium (Supplementary Figure 4e).

We next assessed M19-6 effects against melanoma lines grown in 2D or 3D (spheroid) cultures. Both analyses revealed selective effectiveness of M19-6 against A375, WM793, Mel-5, ZR75-1, and H1693 cells, as well as against BRAF inhibitor-resistant A375 cells, but not against the IGR37, IGR39, Mel28, WM3629 or MeWO cells (Supplementary Figure 4f). To determine whether NRAS or BRAF mutations might confer greater sensitivity to M19-6, we treated melanoma cells harboring these mutations with M19-6. Nras-mutant melanoma cells exhibited greater sensitivity to M19-6 compared with Braf-mutant melanoma cells (Supplementary Figure 4g). Comparable to changes seen in melanoma cells treated with SBI-756 and the parental M19 compound, M19-6 induced more robust S1 arrest and apoptotic effects in melanoma cells, effects that exhibited time dependency (Figure 3d). Spheroids formed from different BRAF or MEK inhibitor-resistant melanoma lines were also M19-6- sensitive (Figure 3e, 3f).

Translatome analysis of M19-6-treated cells

To investigate the impact of M19-6 on mRNA translation, we conducted ribosome profiling (Ribo-Seq) in A375 cells treated 8 hours with M19-6 or vehicle control (Figure 4a). Ribo-Seq, a sequencing-based method, enables genome-wide assessment of mRNA translation efficiency when paired with RNA-Seq [41]. On average, we obtained approximately 37 million and 10 million mapped reads for Ribo-Seq and RNA-Seq, respectively, targeting coding regions of the transcriptome. Micrococcal Nuclease (MNase) digestion generated ribosome footprints with a central peak around 33 nucleotides (nt) (Supplementary Figure 5a). As anticipated, metagene plots of Ribo-Seq data displayed robust accumulation of ribosome footprints within mRNA CDS regions (Supplementary Figures 5b, 5c). Principal component analysis (PCA) of Ribo-Seq and RNA-Seq libraries indicated high reproducibility among biological replicates, with clear separation between M19-6-treated and control samples (Figure 4b). We detected 11,468 and 11,255 highly expressed mRNAs (RPKM > 1) in Ribo-Seq and RNA-Seq datasets, respectively, using the longest CDS for each gene (Supplementary Table 2).

To evaluate translation efficiency in control and M19-6-treated A375 cells, we applied the deltaTE (ΔTE) method [46], an enhanced version of DESeq2 optimized to assess translation efficiency from changes in Ribo-Seq and RNA-Seq data [46, 47] (Figure 4c, Supplementary Table 3). Our analysis identified 104 mRNAs whose translation efficiency was down-regulated by M19-6 treatment (Figure 4c). Notably, most translation efficiency changes fell into the “Exclusive” category, in which mRNA levels remained unchanged, but Ribo-Seq reads were significantly up- or down-regulated (Figure 4c). These findings suggest that M19-6 impacts gene expression primarily through translational regulation.

Among gene ontology (GO) groups translationally down-regulated by M19-6 in A375 cells (p-adj < 0.05 and log2 fold change in TE < -0.5) were mRNAs encoding proteins associated with ribosomal biogenesis, the cell cycle, and translational elongation (Figure 4d, 4e, 4f).

M19-6 ability to eradicate melanoma cells is enhanced with inhibitors of autophagy and histone deacetylase.

To identify activities potentially enhancing M19-6 in promoting melanoma cell death, we re-assessed cellular functions perturbed by M19 treatment based on RNA-seq analysis. Among notable pathways upregulated by M19 treatment was the autophagy gene signature (Supplementary Figures 4c, 4d). Indeed, we observed increased processing of LC3, indicative of autophagic activity, in M19-treated melanoma cells. Thus, we asked whether inhibiting autophagy, which should augment cell survival pathways following M19 treatment, would enhance melanoma cell death promoted by M19-6. To do so, we co-treated melanoma cells with M19-6 and with the autophagy inhibitor chloroquine (CQ; [48]). Notably, we observed dose-dependent synergy between CQ and M19-6 in decreasing melanoma spheroid survival. Moreover, effective inhibition of melanoma spheroid growth required an approximately 4-fold lower concentration of M19-6 (5 μM) relative to single drug treatment in the presence of a relatively low (1.25 μM) CQ dose (Figure 5a).

Given that CQ was rationalized, we set to perform an unbiased screen to identify possible drugs that could enhance M19-6 activity. To this end, we screened a library of FDA-approved drugs from MedChemExpress (for details see Methods). Of the 14 inhibitors identified in this screen we further assessed 6 that were confirmed. Among them, the HDAC inhibitors Chidamide and CI-994 exhibited the most potent inhibition of melanoma cell viability when combined with M19-6 (Supplementary Figures 4h, 4i). Another HDAC inhibitor, FK-228 (at 5nM), enhanced M19-6 (at 625 nM) to achieve ~70% inhibition; Figure 5b). Further assessment of multiple melanoma lines was performed under normoxic and hypoxic conditions to phenocopy in vivo growth conditions. These comparisons confirmed the cooperation between HDAC inhibitors and 19-6 (Figure 5c). These findings overall indicate the ability of enhancing M19-6 effectiveness by co-targeting select cellular pathways including autophagy and histone deacetylases. In both cases, the M19-6 concentration required for cooperation was markedly reduced (relative to concentrations required for its activities as a single agent).

Next, we assessed the M19-6 stability in assays conducted in mouse hepatocytes. We found that M19-6 exhibited a greater T1/2 (19.27 min) and a metabolic stability of 12.92% after 30 min, relative to 11.33 for Verapamil, a drug commonly used to treat hypertension (Supplementary Table 4).

To evaluate effectiveness of combining M19-6 with FK228 to eradicate melanoma cells *in vivo,* we used different *in vivo* models, namely, C3H mice inoculated with SW1 melanoma cells (which harbor an Nras mutation [49-51] and C57BL/6J mice inoculated with B16F10 or YUMM1.5 melanoma cells. Specifically, we treated both models with the combination of M19-6 (90 mg.kg, daily injection) and FK228 (50 ug/kg three times per week). While M19-6 treatment decreased tumor growth, combining it with FK228 did not inhibit tumor growth to a greater extent than FK228 treatment alone (Figure 6a). Notably, M19-6 treatment sufficed to inhibit spontaneous melanoma metastasis to the lungs, which can be assessed in the SW1 model (Figure 6a, right panel). Subsequently, we analyzed M19-6/FK228 combination effects in melanoma lines representing different genetic backgrounds, including B16F10 and YUMM1.5. We observed the most potent M19-6 effects (70% inhibition) in B16F10 cells, an effect not enhanced by FK-228 (Figure 6b). Growth of YUMM1.5 melanoma tumors was attenuated by the M19-6/FK228 combination, albeit to a lesser degree (50%, Supplemental Figure 6a), an expected outcome given the greater activity of M19-6 in *N-ras* mutant melanomas.

A recent study suggested that treatment with SBI-640756 (the parental M19-6 drug) induces anti-tumor immune phenotypes [35]. We thus performed immunophenotyping 12 days following melanoma (YUMM1.5) cell inoculation into C57BL/6J mice that were treated with M19-6 (90 mg/kg daily starting 5 days after tumor cell inoculation). We observed no differences in immune cell activation in M19-6- versus control-treated tumors (Supplementary Figure 6b, 6c). Likewise, we observed no difference in immune cell (CD8 T, FOXP3, or NK1 cells) infiltration of tumors at the end of the experiment (Supplementary Figure 6d). Accordingly, we observed no differences in expression of genes implicated in anti-tumor immunity (Supplementary Figure 6e). That 19-6 cannot induce antitumor immunity could be attributed to changes in the chemistry of the new compound, relative to SBI-640756, or to the in vivo analyses performed in our studies.

These observations, together with cell cycle and growth arrest phenotypes seen in M19-6-treated melanoma cells, seen in our RNAseq and Riboseq analyses, led us to assess effects of combining M19-6 with DNA-damaging drugs, which are commonly used in chemotherapy. As a representative of the large class of DNA-damaging agents, we examined effects of combining M19-6 with doxorubicin [52]. Moreover, to assess M19-6 effects on tumor growth and metastasis, we used one-year-old C3H mice for this analysis, given the propensity of melanoma to metastasize in aged mice [53]. Notably, combining M19-6 with doxorubicin enhanced the degree of melanoma growth inhibition relative to either monotherapy (Figure 6c). Significantly, based on size and number of metastatic lesions, the degree of metastasis, which is notable in this mouse model, was effectively inhibited by M19-6 alone and that inhibition was greater in the M19-6/doxorubicin group (Figure 6d). These findings strongly suggest that melanoma growth and metastasis can be effectively attenuated by a small molecule inhibitor of the

translation initiation complex, and that effect can be enhanced when combined with a DNA-damaging agent, as exemplified here by doxorubicin.

Discussion

The eIF4F complex presents challenges as a therapeutic target in cancer since it is essential for the viability of all cells. However, this apparent disadvantage may be exploited, as complex components are generally overexpressed in tumors relative to normal cells (10,12,13). Strong genetic evidence supporting the targeting of eIF4F has come from analysis of mice heterozygous for eIF4E, which are reportedly resistant to cancer development despite exposure to carcinogens [54]. Among the small molecule inhibitors designed to target this complex, a limited number have advanced to clinical trials, with the eIF4A inhibitor eFT226 being a notable example [55]. Thus, this study was designed to fill an unmet clinical need, leveraging our earlier analyses of SBI-756, a small molecule that interacts with eIF4G1 and dissociates the eIF4F complex [8].

Herein, we first discovered that a small molecule inhibitor, SBI-756, binds the MA3 domain of eIF4G1. This finding guided structure-based *in silico* screen that identified M19 and its analog M19-6, novel small molecule inhibitors of eIF4G1. Notably, compared to SBI-756, these compounds demonstrate dose-dependent suppression of melanoma cell proliferation in 2D and 3D culture models. Furthermore, they effectively disrupted the eIF4F complex and inhibited the interaction between eIF4G1 and eIF4A, underscoring their potential therapeutic efficacy. RNAseq analysis of melanoma cells treated with M19 revealed ROS, UPR, and apoptosis signaling activation, indicating that M19 induces cell death programs. Further assessment using Riboseq approach led to the identification of ribosomal structure components that can be linked to growth arrest phenotypes, which were inhibited following treatment with the 19-6 compound, consistent with the sensitization of melanoma cells to cell death in culture and cytostatic phenotypes in vivo, resembling the requirement of other eIF4F inhibitors for structural ribosomal proteins [32].

In a search for pathways that may complement apoptotic signaling, we hypothesized that autophagy may serve as a salvage pathway to rescue tumors from cell death. Indeed, we found that pharmacological targeting of the autophagy pathway combined with treatment with M19 compounds enhanced the extent of melanoma cell death and reduced (4 to 5-fold) the concentration of compounds required to achieve a potent effect. An unbiased screen of >2000 FDA approved drugs was carried out to identify inhibitors that may augment M19-6 activity, leading to the identification of HDAC inhibitors among top candidates. Further assessment using three independent HDAC inhibitors confirmed their synergy with M19-6 in mediating melanoma cell death, while reducing amount of M19-6 inhibitor required to achieve effective inhibition.

Notably, neither of these combinations was found to be effective *in vivo*. Important to note that independent studies demonstrated that eIF4F inhibitors, when tested on their own, are not sufficient to inhibit tumor growth effectively, requiring to augment their activity by combination with other drugs. For example, combining eFT226 with MEK inhibitors reportedly augments eFT226 activity and is more effective than a single agent against Kras-mutant lung tumors [32].

Among the remaining unmet clinical needs is the emerging resistance of tumors to therapy. Notably, M19-6 ability to attenuate eIF4F complex assembly enables it to overcome therapy resistance, consistent with findings made with the SBI-756 [8], M19-6 was shown to be effective against BRAF- and MEK-resistant melanoma, confirming the need for complex dissociation to counteract therapy resistance.

Targeting of the eIF4F complex has been primarily achieved using small molecules that target eIF4E or eIF4A components to block respective cap-dependent translation or helicase activity [7, 13]. Moreover, reluctance to target eIF4G1 has been justified by a lack of structural data or based on its "adaptor-like" function [56]. Indeed, our earlier generation small molecule, SBI-756, is an effective inhibitor of the eIF4F complex, although its toxicity in culture biophysical properties precluded its further development. Of the >140 SBI-756 analogs previously developed, none exhibited activity superior to SBI-756, while its pharmacokinetics was suboptimal. We have now overcome these limitations by identifying the eIF4G1 MA3 domain as the SBI-756 target and used structure-based analysis to identify and characterize a new generation of small molecule eIF4G1 inhibitors. Pharmacological inhibition of eIF4G1 with these inhibitors was more effective than genetic inactivation of the MA3 domain, likely due to the presence of the eIF4G2 isoform, which also harbors the MA3 domain [36]. Indeed, siRNA-based eIF4G2 knockdown (KD) in melanoma cells harboring gRNA-235 potentiated cell death phenotypes seen in the presence of gRNA-235 alone. We anticipate that targeting the MA3 domain by M19-6 will impact both eIF4G isoforms, with limited toxicity, especially at low doses used in culture and the doses used in preclinical models.

Previous studies demonstrated that eIF4G1 inhibition perturbed the cell cycle and DNA repair processes [21], changes also observed in the presence of SBI-756 [8] and the M19 compound series. Disruption in cell cycle is a long-sought goal in cancer research that has guided the development of numerous inhibitors that have reached clinical evaluation; nonetheless, all must be used in combination with reagents that target other cellular pathways to achieve effective and sustained clinical outcomes, as exemplified by CDK4/6 inhibitors [57]. Our discovery of M19-6 compounds highlights the opportunity for combination therapy, where the second drug could be a DNA-damaging agent, demonstrated in our studies with doxorubicin. While used as a mere example, the opportunity to sensitize naïve and drug-resistant tumors to well-characterized DNA- damaging chemotherapies highlights the importance of M19-6 series of compounds identified and characterized herein.

Overall, our work describes the development of the new generation of eIF4G1 inhibitors that target the MA3 domain of the eIF4G1 gene. M19-6 is more effective in *N-ras* mutant melanoma and overcomes resistance to targeted therapies as well as limits metastasis – the most prevalent unmet clinical needs in melanoma management. Exemplified by M19-6, this new class of inhibitors offers advantages over existing eIF4F inhibitors and merits further evaluation in preclinical and clinical models.

Methods and Materials

Methods

Mouse tumor models and ethics

All animal studies were approved by the Institutional Animal Care and Use Committee (IACUC # 21-064) of Sanford Burnham Prebys Medical Discovery Institute and Cedars-Sinai Medical Center (Protocol: IPROTO202400000350) and complied with respective ethical animal testing and regulations. The mice were housed under a 12 h light–dark cycle at controlled ambient temperature (22±1°C) and relative humidity (40–70%). Adequate standard chow and water were available ad libitum via cage lids. Six-week-old and 1 year-old male C3H/HeNHsd mice were purchased from Inotiv and six-week-old male C57BL/6J mice were purchased from Jackson Laboratories, allowed to acclimatize for one week. SW1 cells (8×10^5), B16F10 cells (2.5×10^5), YUMM1.5 cells (1×10^6), suspended in 200 µL sterile PBS were injected subcutaneously into the flanks of mice. When tumor sizes reached ~150 mm^3, mice were sorted into different groups and treated with IP injection of Vehicle or M19-6 (100 mg/kg, twice per day), FK228 (50ug/g, three times per week) and Doxorubicin (5mg/kg, every two days). Mice were maintained in a pathogen-free environment with free access to food. Body weight and tumor volume were measured twice a week. Tumor size was measured with linear calipers and calculated using the formula: ([length in millimeters × (width in millimeters)^2]/2). Mice were sacrificed after 4 weeks, and tumors and lungs were fixed in Z-Fix and paraffin-embedded for immunohistochemistry analysis.

Cell culture

All human and mouse melanoma cells were maintained in high-glucose Dulbecco's modified Eagle's medium (DMEM; Cytiva, Marlborough, MA) with 10% fetal bovine serum (FBS) and 1% penicillin-streptomycin (Cytiva). Cell cultures were maintained at 37^{0}C in 5% CO_2.

Reagents

Compounds used in this study were purchased from ChemBridge (San Diego, CA), Enamine (Monmouth Junction, NJ), and MolPort (Beacon, MA), as indicated. Chloroquine was obtained from Sigma-Aldrich. Compounds were dissolved in DMSO and stored as a 10 mM stock solution at -20°C. Each compound was freshly prepared from the stock solution before use. Compounds used in animal studies were synthesized by Pharmaron (Qindao, China) at >96% purity.

Cell viability assay

All cell lines were seeded in 96-well white plates (5,000 cells in 100 µl per well) or 384-well white plates (500 cells in 50 µL per well) and allowed to attach overnight. Test compounds were serially diluted from 10 mM stock solutions and added to cells. Assays were performed in triplicate, and each microplate included media and DMSO control wells. Cell viability was assessed 72 h after treatment using CellTiter-Glo (Promega) according to the manufacturer's protocol. Cell growth inhibition was calculated as a percentage of DMSO-treated controls.

For the spheroid growth inhibition assay, cells were seeded in 96-well (1000 cells in 100 µl per well) or 384-well (250 cells in 50 µL per well) white Corning spheroid microplates and allowed to grow 24 h to form spheroids. Test compounds were serially diluted and added to each well. Assays were performed in triplicate, and each microplate included media and DMSO control wells. Cell viability was assessed 5 days later using CellTiter-Glo 3D (Promega) according to the manufacturer's protocol. Cell growth inhibition was calculated as a percentage of DMSO-treated controls.

Colony formation assay

Cells were plated in triplicate (500 cells/well) in 6-well plates and allowed to grow overnight before compounds were added. After 1–2 weeks, depending on the cell line, colonies were stained with Crystal Violet solution (Sigma-Aldrich) for 30 min. Plates were rinsed with water, and images were acquired by scanning. Colony number and size were analyzed using Image J software. Colony formation efficiency was calculated relative to the number of colonies in control (DMSO)-treated wells.

Antibodies, Immunoprecipitation, and Western blot analyses

Cells were rinsed with PBS and lysed in lysis buffer (50 mM Tris-HCl, pH 7.4, 150 mM NaCl, 1% NP-40, 1 mM EDTA) containing protease inhibitors and a phosphatase inhibitor cocktail (Thermo Scientific, Waltham, MA). Protein concentration was determined using Coomassie Plus Protein Assay Reagent (Thermo Scientific). Immunoprecipitation (IP) of eIF4A was performed from cell lysates (300 µg) incubated overnight with 10 µg of anti-eIF4A antibodies (BioLegend, San Diego, CA, cat# 666202), followed by incubation with Protein A/G PLUS-Agarose beads (Santa Cruz, SC-2003) for 1 h. Beads were then washed 4 times with lysis buffer, and IP'd proteins were eluted with SDS loading buffer and analyzed by Western blot. Equal amounts of cell lysate proteins (20-50 µg) or proteins eluted from agarose beads were separated on SDS-PAGE and transferred to polyvinylidene difluoride (PVDF) membranes (PerkinElmer Life Sciences). Membranes were blocked 1 h with 3% BSA/TBST and incubated with primary antibodies overnight at 4°C, with shaking. Following three TBST washes, membranes were incubated 1 h at room temperature with secondary antibodies. Detection and quantification were made using an Odyssey Infrared Imaging System (LICOR Biosciences). Antibodies against eIF4G1, eIF4E, and 4EBP1 were purchased from Cell Signaling Technology (cat# 8701, cat# 2067, cat# 9644). Actin and HSP90 antibodies were obtained from Santa Cruz Biotechnology (cat# sc-58673, cat# sc-13119). Secondary antibodies were goat anti-rabbit Alexa Fluor 680 (cat# A21076), goat anti-mouse Alexa Fluor 680 (cat# A21057), and goat anti-rat Alexa Fluor 680) (cat# A21096) (Invitrogen). All antibodies were used according to suppliers' recommendations.

Construction of EIF4G1 tiling sgRNA library

The custom EIF4G tiling sgRNA library consisting of 947 unique sgRNAs was designed using the Broad Institute Genetic Perturbation Platform (GPP) sgRNA designer tool [58-60]. Library sequences were synthesized on an array platform (Genscript, NJ) and then cloned into the lentiGuide Puro vector (Addgene: #52963, a kind gift from Dr. Feng Zhang, MIT) using Golden Gate Assembly. The library plasmid was amplified using ElectroMAX™ Stbl4™ Competent Cells (Invitrogen, cat # 11635018). To ensure representation, the number of bacterial colonies was maintained at >500 times the number of sgRNA sequences in the library. sgRNA sequences in the library are deposited as indicated in the data availability section.

Selection of SBI-756-resistant clones and identification of corresponding gRNAs

The pooled tiling CRISPR library virus was produced using HEK293T cells transfected with pMD2.G and psPAX2 in the presence of Polyethylimine (PEI). A375 cells (2 x 10^6) were then transduced with the pooled library lentivirus in DMEM complete medium and 0.8 µg/ml

polybrene. Twenty-four hours later, virus, polybrene, and medium were removed, and cells were plated in fresh culture medium. Forty-eight hours after that, puromycin was added at 1 µg/ml to select for sgRNA library-expressing cells. The multiplicity of infection (MOI) was adjusted to 0.3-0.4 to prevent >1 sgRNA infection per cell. Cells were cultured at >1,000X of the library size to ensure adequate sgRNA representation. Cells were treated with indicated SBI-756 concentrations for 2-4 weeks until resistant clones emerged. Genomic DNA extraction from drug-resistant cells was performed using the Zymo QuickDNA™ Midiprep Plus Kit (Zymo Research, Cat # D4068), according to the manufacturer's instructions.

gRNA sequencing data processing

A two-step PCR-amplification for sequencing library preparation was conducted with TaKaRa Ex Taq™ Polymerase (TaKara, Cat. RR001) and custom primers, to achieve adequate sequencing coverage in 1x75bp single-end reads, following published guidelines [61]. Barcoded libraries were pooled and sequenced using an Illumina Hiseq 500 platform.

CRISPR screen data analysis:

The sequence and Pfam domains of the longest transcript of EIF4G1 gene (ENST00000424196.5) was obtained from the Ensembl database. Raw reads were sequentially trimmed for 3' and 5' adapters using Cutadapt v2.8 with parameters "-j 4 -e 0.15 -a GTTTTAGAGCTAGAAATAGCAAGTTAAAATAAGGCTAGTCCGTTATCAAC" and "-j 4 -e 0.15 -m 18 -g TTTATATATCTTGTGGAAAGGACGAAACACCG" respectively. The trimmed reads were aligned to EIF4G1 longest transcript sequence using STAR v2.7.0d_0221[62]) with parameters "--runThreadN 8 --alignEndsType EndToEnd --outFilterMismatchNmax 0 --outFilterMultimapScoreRange 0 --outReadsUnmapped Fastx --outSAMtype BAM Unsorted--outFilterMultimapNmax 1 --outSAMunmapped None --outFilterScoreMinOverLread 0 --outFilterMatchNminOverLread 0 --outFilterMatchNmin 20 --alignSJDBoverhangMin 1000 --alignIntronMax 1". Signal bigwig files were generated using Deeptools bamCoverage v3.2.0[63] with parameters "—normalize using CPM --exactScaling".

Selection of single-cell gRNA clones

Individual gRNA235 or gRNA622 virus was produced using 293T cells following standard protocols and used to infect A375 cells following puromycin selection (1 µg/mL). Single-cell

clones were generated by serial dilution (0.2 cell/100 µL) in 96-well plates. The resulting single-cell clones were treated with SBI-756, and resistant clones were selected. Genomic DNA was extracted from selected clones, and the region corresponding to the gRNA was PCR-amplified and sequenced to confirm specific deletion at the targeted region.

m^7GTP pull-down assay

Cells growing in 100 mm plates and treated with indicated compounds were washed with cold PBS, collected, and lysed in lysis buffer [50 mM MOPS/KOH (pH 7.4), 100 mM NaCl, 50 mM NaF, 2 mM EDTA, 2 mM EGTA, 1% NP40, 1% Na-DOC, 7 mM β-mercaptoethanol containing protease inhibitors and a phosphatase inhibitor cocktail). Lysates were incubated 20 min with m^7-GDP-agarose beads (Jena Bioscience, Jena, Germany) with rotation and washed three times with wash buffer (50 mM MOPS/KOH, pH 7.4, 100 mM NaCl, 50 mM NaF, 0.5 mM EDTA, 0.5 mM EGTA, 7 mM β-mercaptoethanol, 0.5 mM PMSF, 1 mM Na3VO4 and 0.1 mM GTP). Bound proteins were eluted by incubating beads in a loading buffer. Materials pulled down by m^7-GDP-agarose were analyzed by Western blot.

Monitoring of newly synthesized proteins by puromycin labeling

For labeling experiments, A375 cells were seeded in 6-well plates (3 x10^5 cells per well). After 24 h, cells were pre-incubated 1 h with different compounds prior to treatment with 3 µg/mL puromycin for 30 min. Cells were washed 2 times with ice-cold PBS and lysed with lysis buffer. Cell lysates were subjected to Western blot analysis.

Histology and immunofluorescence.

Tumors and lung were collected by the end of the experiment. Tissues were fixed with 4% formalin, washed with PBS, embedded in paraffin and cut in 5 µM-thick sections and stained with H&E. For immunofluorescence, the tissues were deparaffinized, rehydrated and washed with PBS. Antigen retrieval was performed using Epitope Retrieval Solution pH 6 (Leica Biosystems). Sections were incubated at 4°C overnight with CD8α (Cell signaling technology, Clone: D4W2Z, dilution: 1:500), NK1 (Cell signaling technology, Clone: E6Y9G, dilution: 1:150), FOXP3 (Invitrogen, Clone: FJK-16s, dilution: 1:200). The antibodies were diluted in Dako antibody diluent. Then, the slides were washed with PBS and incubated 2 hours at room temperature with Alexa Fluor 594-conjugated and Alexa Fluor 488-conjugated with secondary antibodies. Nuclei were stained with SlowFade Gold Antifade reagent with 4',6-diamidino-2-phenylindole (DAPI, Vector). Data were obtained using Leica DMi8 Fluorescence microscope.

Tumor digestion.

Tumors were harvested at day 12 after tumor injection and digested with 100 µg/mL DNase I (sigma) and 1mL of collagenase D (Roche) at 37°C for 1 hour. To generate single-cell suspension, the tumor digested was passed through a 70 µm cell strainer. The cells were washed with PBS and incubated with the indicated antibodies for flow cytometry.

Flow Cytometry analysis of tumor cells.

Tumor single cells were washed with FACS staining buffer and incubated with antibodies (dilution 1:200) at 4°C for 20 min and fixed using 1% of formaldehyde in PBS for 20 min, followed by washed before resuspending in FACS staining. The antibodies were used were: NK1.1 (Clone: OK136), CD8 (Clone: 53-6.7), CD4 (Clone: RM4-5), Lag3 (Clone: C9B7W), CD69 (Clone: H1.2F3), B220 (Clone: RA3-6B2), CD44 (Clone: IM7), CD45 (Clone: 104), CD279 (Clone: 29F.1A12), MHC II (Clone: M5/114.15.2), CD11b (Clone: M1/70), PDCA-1 (Clone: 129c1), CD11c (Clone: N418), MHC I (Clone: AF6-88.5), F4/80 (Clone: BM8), CD206 (Clone: C068C2), GR1 (Clone: RB6-8C5), CD80 (Clone: 16-10A1), TCF-1 (Clone : S33-966), TIM-3 (Clone : B8_2C12). All the data were collected on an BD FACSymphony A5 and analyzed using Flowjo Software.

Analysis of the cell cycle.

A375 cells that express the gRNA constructs were subjected to FACS analysis following their trypsinization, fixation (60 min in 70% ice-cold ethanol), and washes in phosphate-buffered saline, followed by incubation for30 min at 25°C in propidium iodide (PI) buffer (10 mM Tris-HCl, pH 7.4, 5 mM MgCl2, 50 µg of PI per ml, and 10 µg of RNase A/ml). Stained cells were acquired using the FACSort flow cytometer (BD Biosciences), and DNA content was analyzed using FlowJo software.

Analysis of apoptosis and ferroptosis

A375 cells were seeded in 96- or 384-well white plates, treated with different concentrations of indicated compounds, and apoptosis was measured at different time points using Caspase-Glo 3/7 (Promega, G8091), according to the manufacturer's protocol. Caspase-Glo 3/7 3D (Promega, G8981) was used to analyze A375 spheroid apoptosis induced by different treatments.

Reverse transcription and real-time qPCR

Total RNA from DMSO- and compound-treated cells, and tumors was extracted using a total RNA miniprep kit (Zymo Research). cDNA was synthesized using a High-Capacity cDNA Reverse Transcription Kit from Life Technologies, according to the manufacturer's protocol. Real-time PCR was performed on a Bio-Rad CFX Connect Real-Time System using SsoAdvanced Universal SYBR®Green Supermix from Bio-Rad. H3A served as an internal control. Quantitative PCR reactions were performed in triplicate. PCR primers were designed using PrimerBank (http://pga.mgh.harvard.edu/primerbank) and are listed (Supplementary Table 3).

Polysome profiling

A375-gRNA235 and A375-gRNA622 cells were seeded in 150 mm plates and treated with 0.2 µM SBI-756. After 24 h, cells were harvested and lysed in hypotonic lysis buffer (5 mM Tris HCl, pH 7.5, 2.5 mM MgCl2, 1.5 mM KCl, 100 µg/ml cycloheximide, 2 mM DTT, 0.5% Triton, 0.5% sodium deoxycholate). Polysome-profiling was carried out as described [42]. Fractions were collected, and RNA was extracted using TRIzol, based on the manufacturer's instructions. Experiments were done in independent triplicate samples.

RNA-seq

Total RNA was extracted using a total RNA miniprep kit (Sigma) with the supplied On-column DNase I for the digestion step. Libraries were prepared from isolated total RNA using the QuantSeq 3' mRNA-Seq Library Prep Kit FWD for Illumina (Lexogen, Vienna, Austria). Barcoded libraries were pooled and single end-sequenced (1X75) on the Illumina NextSeq 500 system, using the High output V2.5 kit (Illumina Inc., San Diego, CA). Read data was processed and multiplexed with the BlueBee Genomics Platform (BlueBee, San Mateo, CA).

RNA-seq data processing

The Illumina adapter, polyA/polyT and low-quality sequences were trimmed from raw RNA-seq reads using Cutadapt v2.3. The trimmed reads were then aligned to human genome version hg38 and Ensembl gene annotations version 84 using STAR v2.7.0d_0221[62] with parameters adopted from ENCODE long RNA-seq pipeline (https://github.com/ENCODE-DCC/long-rna-seq-pipeline). Gene-level counts and normalized expression (TPM) were obtained using RSEM v1.3.1 [3]. Trimmed reads and alignment qualities were assessed using FastQC v0.11.5

(https://www.bioinformatics.babraham.ac.uk/projects/fastqc/) and MultiQC v1.8 [64]. Genes with RSEM-estimated counts equal to or greater than 5 times the total number of samples were retained for downstream analysis. Differential expression comparison was performed using DESeq2 v1.22.2 [47]. Gene set enrichment analysis was performed using the GSEA app v4.3.2 [65]

In silico screen for MA3-bound small molecules

To map SBI-756 binding to the MA3 structure, a blind docking technique (molecular docking without a defined target site) was first performed using Glide[66] and FRED docking software[67]. This analysis revealed a potential site where SBI-756 formed stable bonds during a 30ns molecular dynamics simulation performed with the Desmond suite from Schrodinger [44].

To identify small molecule inhibitors of eIF4GI, we carried out a virtual screen of the MA3 binding pocket. Based on molecular docking of a large library with subsequent filtering [45], a screen with a library of 10 million drug-like compounds (deposited in the ZINC20 database; [68] was carried out. Compounds were docked in the pocket based on three docking software systems, namely, GlideSP [66], FRED [67], and Autodock [69 , 70, 71], which were shown to improve hit rates [72, 73]. Binding poses predicted by these systems were compared, and compounds with consensus predictions (binding poses within 3Å distances) were selected. These compounds were ranked based on Glide docking scores. A total of 54,500 compounds received a more favorable docking score than the predicted SBI-756 with the docking score of -4.7. As SBI-756 presents an active scaffold targeting the MA3 pocket, we utilized its structure to build pharmacophore models to screen the filtered library to identify molecules with SBI-756-like binding features that lacked SBI-756 toxicity. Developed pharmacophore models contained three hydrophobic features corresponding to each of the three separate SBI-756 ring systems—one hydrogen donor and one hydrogen acceptor corresponding to the nitrogen and oxygen atom of the quinolone group. These features were used in different combinations to screen the filtered library and select 500 chemically diverse compounds. Finally, we selected compounds with drug-like physicochemical properties less likely to promote toxicity and exhibit off-target binding, based on empirical and machine learning-based methods. To this end, we first applied Andrew's scoring metric, which assesses how well a molecule binds to an average receptor, by assigning partial scores to each functional group in the molecule [72, 73]. Potentially promiscuous compounds with a high Andrew's score were eliminated. SBI-756 appeared in the top 10th percentile among the 500 scored compounds and thus is likely toxic due to its general receptor promiscuity, consistent with our earlier studies [74]. Second, we ran the remaining compounds through the Swiss-ADME platform to predict physicochemical properties and potential off-target effects [73]. Compounds predicted to inhibit 5 or 6 CYP family enzymes,

which are critical for drug metabolism and clearance [75], were filtered out. Compounds receiving predicted log P values (lipophilicity) <5 were selected, as highly lipophilic compounds tend to be more promiscuous and are minimally soluble [76]. Compounds with low solubility in aqueous media (log S < -6) were excluded to avoid low bioavailability. SBI-756 was predicted to be on the borderline of lipophilicity and solubility scales, receiving 4.6 and -5.18 scores, respectively. The remaining 150 compounds were clustered, and cluster representatives were selected. Clustering procedures ensure that the purchased compound set is as chemically diverse as possible, maximizing the likelihood of finding an active scaffold. 67 potential inhibitors that bind the MA3 pocket were selected for biological evaluation.

Ribosome Profiling

Cultured cells were lysed in-dish using 250 µL of 2X lysis buffer, containing 40 mM Tris-HCl (pH 7.4), 300 mM NaCl, 10 mM $MgCl_2$, 200 µg/mL cycloheximide (CHX), and 2 mM dithiothreitol (DTT), supplemented with Complete™ Protease Inhibitor Cocktail. Lysed cells were scraped into an Eppendorf tube (~500µL), 5 µL of RiboLock RNase inhibitor (ThermoFisher Scientific, Cat#EO0382), and 5 µL of Turbo DNase (ThermoFisher Scientific, Cat#AM2238) were added to each lysate. The mixture was vortexed briefly (5 sec), incubated on ice for 10 minutes, and then centrifuged at 16,000× g for 10 minutes at 4°C. The optical density was recorded at A260 using a Nanodrop to assess concentration. Samples were stored at -80°C, with a portion reserved for RNA-Seq prior to Micrococcal Nuclease (MNase) treatment.

For ribosome profiling, lysates underwent MNase digestion (25U MNase (Sigma) per A260 unit) for 45 minutes at room temperature. The digestion was halted by adding EGTA. Monosomes were isolated by layering the digested polysomes over a 10-50% sucrose gradient, followed by centrifugation at 36,000 rpm for 3 hours at 4°C (Beckman Coulter). RNA was then extracted from the monosomes fraction using Trizol (Invitrogen) as per the manufacturer's guidelines. In parallel, total RNA was extracted with Trizol from a portion of the untreated lysate for RNA-seq analysis.

For Ribo-seq library preparation RNA samples were size-selected on a 15% TBU-Urea gel, with fragments between 25–40 nt isolated. The gel slices containing these fragments were incubated in 700 µL of RNA gel extraction buffer (300 mM NaOAc pH 5.5, 1 mM EDTA, 0.25% SDS) on dry ice, then rotated overnight at room temperature. Footprint fragments were recovered via isopropanol precipitation. The ribosome footprints were dephosphorylated with T4 Polynucleotide Kinase (T4 PNK) for 1 hour at 37°C in 1X T4 PNK buffer, with the addition of 10 U SUPERase*In and 5U T4 PNK (10 U/µL). Ligation was achieved by adding the ligation mix (17.5% PEG-8000, 1X T4 RNA ligase buffer, 100 U T4 Rnl2(tr) K227Q (200 U/µL), and 1 µM pre-adenylated linkers) to the samples. Ligated RNA was separated on a 10% TBE-Urea gel, extracted, and purified using RNA extraction buffer and isopropanol. Reverse transcription was conducted with SuperScript III (Invitrogen), and samples were circularized with CircLigase I

(Lucigen). A round of rDNA depletion was performed using biotin-labeled antisense probes and Dynabeads MyOne Streptavidin C1 [77]. The final libraries were size verified on an 8% TBE gel, quantified, and sequenced on an Illumina Platform.

For RNA-seq library preparation, the same protocol was applied, with modifications. The NEBNext® rRNA Depletion Kit (Human/Mouse/Rat) was used for rRNA removal, and the rRNA-depleted RNA was fragmented using the NEBNext® Magnesium RNA Fragmentation Module.
To process sequencing data, initial trimming of adapters from reads was conducted with Cutadapt 3.4, allowing no mismatches in adapter sequences, and discarding reads shorter than six nucleotides. Trimmed reads were then demultiplexed by sample-specific barcodes anchored at the 5' end, with no mismatches permitted. Sequential alignment was performed against the human transcriptome, beginning with cytoplasmic and mitochondrial rRNAs and tRNAs, using Bowtie 1.3.0 [78]. Reads with low quality or shorter than 25 nucleotides were removed. Remaining reads were aligned to the comprehensive transcriptome (Gencode v32[79] with Bowtie 1.3.0, allowing two mismatches. The SAM files generated were converted to BAM files, sorted, indexed, and processed to remove PCR duplicates with UMI-Tools 1.0.1 [80]. The final BAM files were converted into an SQLite format for analysis in Trips-Viz, a dedicated platform for Ribo-seq data [81]. For metagene profile generation, annotated start and stop codons of coding sequences were aligned across all principal transcript isoforms by read length. To estimate the A-site position of each read, we calculated the nucleotide distance from the CDS start to the most prominent peak upstream, adding three nucleotides to this value.

Differential Expression Analysis

Count matrices for RNA-Seq and Ribo-Seq data were generated using the “Read Table” function in Trips-Vis [81], which quantifies reads that uniquely align to the CDS region of mRNAs based on inferred A-sites. A Ribo-Seq read contributes to the CDS count if its inferred A-site falls within the annotated start and stop positions of the CDS in a given transcript. The genomic coordinates for each read were assessed to ensure unambiguous mapping. Differential analysis was conducted with the deltaTE (ΔTE) package in R (version 1.34.0; [46], which extends DESeq2 by applying an interaction model. For each gene, adjusted p-values (p-adj) were computed to assess fold changes between two experimental conditions across Ribo-Seq, RNA-Seq, and TE levels, with a significance threshold of p-adj < 0.05 for each fold change. These fold changes allowed categorization of genes into eight groups, as described in the text. In the scatter plots for fold changes between Ribo-Seq and RNA-Seq (Figure 4C), genes with “NA” values in any of the comparisons (Ribo-Seq or RNA-Seq) were omitted. PCA plot values in Figure XB were also obtained using DESeq2.

Hepatocyte stability assay

A hepatocyte stability assay was performed by Pharmaron (Beijing, China). Briefly, mouse hepatocytes (0.5×10^6/ml) were dispensed into microtubes and 10 µL aliquots incubated (10 min) with the test compound (100 µM) or Verapamil (positive control; 100 µM), followed by incubation with 6 volumes of cold acetonitrile with IS (100 nM alprazolam, 200 nM labetalol, 200 nM caffeine and 200 nM diclofenac) to terminate the reaction. Samples were then centrifuged (45 minutes at 3,220 g), and 100 µL aliquots of supernatants were diluted with 100 µL ultra-pure H_2O, for LC/MS/MS analysis.

Screen for FDA approved drugs that augment M19-6 activity

The Cell Titer-Glo Luminescent Cell Viability Assay (Promega) was utilized to measure viability of A375 melanoma cells after their treatment with M19-6 in combination with compounds from the MedChemExpress, an FDA-Approved small molecule drug library. To optimize screening conditions, five different cell concentrations were tested alongside their tolerance to DMSO. Ultimately, a concentration of 1,000 cells per well with less than 2.5% DMSO was selected for the assay. A titration of M19-6 was then performed, to establish a baseline concentration for the screening process, which was set to achieve cell viability at 70% after 48 hours. The library was then screened at 6.25 µM (for each of the library compounds), using M19-6 at 40 µM. Cells treated solely with M19-6 were considered as the negative control (0% activity), while wells containing only media (without cells) served as the positive control (100% activity). Compounds were ranked based on their percent activity, resulting in 81 hits selected for further testing. The selected compounds underwent a five-point dose-response assessment (25, 12.5, 6.25, 3.125, and 1.5625 µM) in triplicate, both with and without M19-6 at 40 µM. In this analysis, 14 compounds demonstrated dose-dependent activity and an increased IC50 in the absence of M19-6, leading to their selection for a more extensive dose-response evaluation. The latter consisted of a 15-point dose response with a 1:2 dilution factor starting at 100 µM (100, 50, 25, etc.), and was conducted in triplicate with and without M19-6 (40 µM).

Statistics and Reproducibility

Statistical significance was assessed by ordinary one-way ANOVA and two-way ANOVA. GraphPad Prism 9 software (GraphPad, La Jolla, CA) performed all statistical calculations. All cell culture experiments were performed three times. Data is presented as mean ± SD (unless noted otherwise in figure legends). A P value <0.05 was considered statistically significant.

Primer information

ATF4: Forward, 5'-ATGACCGAAATGAGCTTCCTG-3'; Reverse, 5'-GCTGGAGAACCCATGAGGT-3'

XBP1: Forward, 5'-AGAAGTCCGTCCACTCTCTCA-3'; Reverse, 5'-GCTCGGGATTTTACCAGTTCAT-3'

DDIT3: Forward, 5'-GGAAACAGAGTGGTCATTCCC-3'; Reverse, 5'-CTGCTTGAGCCGTTCATTCTC-3'

HSPA5: Forward: 5'-CATCACGCCGTCCTATGTCG-3'; Reverse, 5'-CGTCAAAGACCGTGTTCTCG-3'

ERN1: Forward: 5'-AGAGAAGCAGCAGACTTTGTC-3'; Reverse, 5'-GTTTTGGTGTCGTACATGGTGA-3'

PPP1R15A: Forward, 5'-ATGATGGCATGTATGGTGAGC-3'; Reverse, 5'-AACCTTGCAGTGTCCTTATCAG-3'

EIF2AK3: Forward, 5'-GGAAACGAGAGCCGGATTTATT-3'; Reverse, 5'-ACTATGTCCATTATGGCAGCTTC-3'

CYP1A1: Forward, 5'-TCGGCCACGGAGTTTCTTC-3'; Reverse: 5'-GGTCAGCATGTGCCCAATCA-3'

HERPUD1: Forward, 5'-TGCTGGTTCTAATCGGGGACA-3'; Reverse, 5'-CCAGGGGAAGAAAGGTTCCG-3'

HMOX1; Forward, 5'-AAGACTGCGTTCCTGCTCAAC-3'; Reverse, 5'-AAAGCCCTACAGCAACTGTCG-3'

JUN: Forward, 5'-TCCAAGTGCCGAAAAAGGAAG-3'; Reverse, 5'-CGAGTTCTGAGCTTTCAAGGT-3'

TGFB2: Forward, 5'-CAGCACACTCGATATGGACCA-3'; Reverse, 5'-CCTCGGGCTCAGGATAGTCT-3'

PPP2R2B: Forward, 5'-CCACACGGGAGAATTACTAGCG-3'; Reverse, 5'-TGTATTCACCCCTACGATGAACC-3'

WNT7B: Forward, 5'-GAAGCAGGGCTACTACAACCA-3'; Reverse, 5'-CGGCCTCATTGTTATGCAGGT-3'

IL1B: Forward, 5'-ATGATGGCTTATTACAGTGGCAA-3'; Reverse, 5'-GTCGGAGATTCGTAGCTGGA-3'

ATF3: Forward, 5'-CCTCTGCGCTGGAATCAGTC-3'; Reverse, 5'-TTCTTTCTCGTCGCCTCTTTTT-3'

Data Availability

All data needed to evaluate the conclusions in the paper are present in the paper and/or the Supplementary Materials. Additional information may be requested from the corresponding author. RNAseq raw data has been deposited in a public database (GSE-271201).

Acknowledgments

We thank the SBP Vivarium for helping with animal studies, the SBP Genomics core for assistance with RNAseq, and Chi-Chang Yang for helping with the analysis of MA3 mutant clones. Support by NCI grant P30 CA030199 enabled the contributions of shared resources to different aspects of this study. NIH support through grant R35 CA283706 and a grant from the Melanoma Research Foundation (to ZAR) are gratefully acknowledged. I.T. is a Senior Research Scholar of the Fonds de Recherche du Quebec–Sante (REQ-S).

Author contributions:

YF, NS, IT, HK, and ZAR designed the studies; YF, XDO, and HJ performed the experiments. RM and HK carried out bioinformatic analyses of RNAseq. MR and AC performed *in silico* screens. SO, ES, and MJ carried out small molecule screens and medicinal chemistry for select compounds. AD generated the eIF4G1 CRISPR library, and IL performed a screen for SBI-756 resistance in yeast. MA, CD, and NS carried out polysome sequencing. IT and PJ carried out polysome profiling. JV provided MEK-resistant melanoma cells. AM performed a pathological analysis of melanoma metastasis. NS, IT, AC, CF and ZAR provided critical data assessments. ZAR, IT, MA, NS, AC, HK, and SO wrote the manuscript.

Conflict of Interest

ZAR is a co-founder and consultant for Pangea Biomed. All other authors declare no competing financial interests.

Materials & Correspondence

Correspondence and requests for materials should be addressed to Ze'ev A. Ronai, Department of Biomedical Sciences and Jim and Eleanor Randal Departament of Surgery, Translational Research Institute, Cedars Sinai Medical Center, 8700 Beverly Blvd. Los Angeles, CA, 90048, T- 310-423-4248, E – zeev.ronai@cshs.org

Figure Legends

Figure 1. Identifying MA3 domain as SBI-756 target on eIF4G1

CRISPR screen identifies eIF4G1 domains targeted by SBI-756. A CRISPR library of sgRNAs prepared against different eIF4G1 gene domains was used to transduce A375 and UACC903 human melanoma cells, which were then treated with puromycin to select for sgRNA-expressing cells and with increasing SBI-756 concentrations. (a) Genomic DNA from cells was PCR-amplified and Sanger-sequenced. Count #s of reads was mapped to each sgRNA. Two enriched sgRNAs (gRNA-235 and gRNA-622) were mapped to the eIF4G1 MA3 domain. gRNA-235 falls within the MA3 domain and results in early termination (aa 1322 of 1606) and thus excludes the W2 domain, which reportedly interacts with eIF4A, from this transcript. gRNA-622 is located proximal (upstream) of the MA3 domain. (b) MA3 mutant melanoma cells are more resistant to SBI-756 than parental MA3 domain WT melanoma cells. gRNA-235 and gRNA-622 melanoma cells obtained as described in Methods were treated with indicated concentrations of SBI-756, followed by the analysis of their viability (72h later) using CellTier-Glo. (c) M^7GTP pull-down assay. Proteins prepared from gRNA-235, gRNA-622 A375 melanoma cells that were treated with indicated SBI-756 concentrations were incubated with m^7GTP-agarose beads to capture the eIF4F complex. Indicated proteins were detected by Western blot analysis. Each protein band was quantified by ImageJ, normalized to eIF4E levels as indicated. Right panel shows the total cell lysate. Each protein band was quantified by ImageJ, normalized to actin levels as indicated. (d) Proteins prepared from EV, gRNA-235 and gRNA-622 A375 cells were immunoprecipitated with eIF4A antibody and detected with indicated antibodies. (e) Polysome profiling of human melanoma A375 cells harboring WT eIF4G1 or eIF4G1 with a mutant MA3 domain (sg235 and sg622), prior to and after SBI-756 treatment. Three replicates are shown, as is the polysome/monosome ratio (right panels).

Figure 2. In Silico screen to identify MA3 domain bound small molecules

(a) The proposed binding mode of SBI-756 to the surface of the eIF4G1 MA3 domain. Left, high-view of SBI-756 binding to the MA3 domain (PDB: 1UG3). Green areas, hydrophobic patches; red areas, solvent exposed. Right, ligand-protein interactions of SBI-756 inside the proposed pocket. Blue shading, solvent-exposed; lines with arene symbols, hydrophobic interactions; arrowed lines, hydrogen bonds. Bonds shown were maintained throughout the 30ns molecular dynamics simulation. (b) A375 and H3A cells were seeded in 96-well plates and treated with different concentrations of indicated compounds. Cell viability was measured after 72 h. (c) A375 cells were treated as indicated. After 24 h, cells were harvested followed by proteins extraction, immunoprecipitation and Western blot analysis with indicated antibodies. Each protein band was quantified by ImageJ, normalized to eIF4A levels as indicated. (d) Proteins prepared from A375 cells treated as indicated were incubated with m^7GTP-agarose beads to

capture the eIF4F complex. Indicated proteins were detected by Western blot analysis. Each protein band was quantified by ImageJ, normalized to eIF4E levels as indicated.

Figure 3. RNAseq analysis of M19-treated melanoma and characterization of M19 analogs.

(a) Volcano plot comparing the transcriptomes of M19 treated and control A375 samples. The numbers of up- and down-regulated genes are indicated in the top corners. Representative genes that were up- or down-regulated upon treatment are denoted. (b) A375 and H3A cells were seeded in 96-well or 384-well Corning spheroid microplates. After 24h, indicated compounds were added to respective wells and cell viability was measured after 4 days using CellTiter-Glo 3D. (c) M^7GTP pull-down assay and immunoprecipitation assay. Left, proteins prepared from A375 cells treated with indicated compounds were incubated with m^7GTP-agarose beads to capture the eIF4F complex. Indicated proteins were detected by Western blot analysis. Each protein band was quantified by ImageJ, normalized to eIF4E levels as indicated blow blots. Right, proteins prepared from A375 cells treated with indicated compounds were incubated with anti-eIF4A antibody followed by Western blot analysis. Each protein band was quantified by ImageJ, normalized to eIF4A levels as indicated. (d) Left, A375 cells were treated with indicated concentrations of M19-6. After 24h, cells were collected and fixed followed by FACS analysis. Right, A375 cells were treated with indicated concentrations of M19-6. Apoptosis was measured using caspase-Glo 3/7 kit. (e) and (F) BRAF inhibitor-resistant and MEK inhibitor-resistant cell lines were grown as spheroids and treated with M19-6. Cell viability was measured after 4 days.

Figure 4: Translatome of M19-6 compound in A375 cells

(a) Schematic illustrating the experimental workflow for RNA-Seq and Ribo-Seq library preparation and sequencing in A375 cells. Biological replicates of A375 cells were treated with a control compound or M19-6 for eight hours prior to analysis. (b) Principal Component Analysis (PCA) of Ribo-Seq (left) and RNA-Seq (right) datasets, showing clear segregation by treatment. Each circle represents a biological replicate, with treatments color-coded for distinction. (c) Scatter plot depicting the relationship between fold changes (FC) in RNA-Seq and Ribo-Seq data for control versus M19-6-treated cells. Statistically significant mRNAs (p-adj < 0.05, Log2 FC > 0.2 or < -0.2) are categorized and color-coded as follows: *Intensified Up* (increased transcription and translation efficiency [TE]), *Intensified Down* (decreased transcription and TE), *Forwarded Up* (concurrent increases in mRNA and RPF with unchanged TE), *Forwarded Down* (concurrent decreases in mRNA and RPF with unchanged TE), *Exclusive Up* (increase in RPF and TE without mRNA change), *Exclusive Down* (decrease in RPF and TE without mRNA change), *Buffered Up* (decreased transcription/increased TE), and *Buffered Down* (increased transcription/decreased TE). (d) Gene Ontology (GO) enrichment analysis of translationally

down-regulated mRNAs in M19-6-treated cells compared to control, with p-values adjusted for multiple comparisons via the Benjamini–Hochberg method. Down-regulated mRNAs with p-adj < 0.1 and -0.5 < Log2 FC < 0.5 were included in this analysis, with n = 49. (e) heat map of genes implicated in ribosome biogenesis which were enriched (f) heat map of genes implicated in cell cycle control which were enriched.

Figure 5. M19-6 combination inhibits melanoma growth in culture.

(a) A375 cells were seeded in 384-well Corning spheroid microplates and treated 24h later with indicated concentrations of M19-6 and chloroquine. Cell viability was measured after 4 days using CellTiter-Glo 3D. (b) Cells were studied as indicated in panel A except of using M19-6 with the HDAC inhibitor FK-228. (c) Analyses of HDAC inhibitor (FK-228) with M19-6. B16F10, YUMM1.5 and SW1 cells were seeded in 384-well plates and 24h later, M19-6 and FK-228 were added to respective wells at the indicated concentrations under normoxia and 6% oxygen. Cell viability was measured after 72h days using CellTiter-Glo.

Figure 6. M19-6 combination inhibits melanoma growth and metastasis in vivo.

(a) SW1 cells grafted into 8 weeks old C3H/HeNHsd mice (n=10) subjected to treatment with M19-6, FK228 and their combination (M19-6 + FK228). Shown is the size and growth of the SW1 tumors and lung metastases (right panel) (b) B16F10 cells were inoculated in C57BL/6 mice (n=10 per experimental group) that were subjected to treatment with M19-6, FK228 and their combination (M19-6 + FK228). Shown is the growth and weight of B16F10 tumors. (c) SW1 cells were grafted into 1 year old C3H/HeNHsd mice (n=10 per experimental group), which are more susceptible for metastasis development, following their treatment with M19-6, doxorubicin and their combination (M19-6 + doxorubicin). Tumor size measurements were performed at the indicated time points. (d) Metastasis of SW1 tumor cells grafted into 1 year old C3H/HeNHsd mice. Shown is quantification of lung macro metastasis in each of the treatment groups (n=10 per experimental group).

Supplementary Figure Legends

Supplementary Figure 1. Identifying MA3 domain as SBI-756 target on eIF4G1.

(a) A375 and UACC903 melanoma cells were subjected to indicated sgRNA infection followed by treatment with SBI-756. Genomic DNA was extracted from the cells followed by sequencing. eIF4G1_sgRNA-235 and sgRNA-622 counts were shown. (b) MA3 domain sequences of gRNA-235 and gRNA-622 A375 cells. sgRNA sequence shown in green and MA3 sequence in red.

Deleted nucleotides are double strikethrough. (c) Left, KY775 strain was transformed with an empty vector or a vector coding for TIF1. Transformed cells were grown with DMSO or 1.25µM SBI-756 for 48h before assessing the cell number by optical density. Data were normalized to DMSO treated cells. Error bars represent sem, n=3. Significance was assessed by Student's T test: **: p-value < 0. Right, KY775 strain was transformed with a library of randomly mutated TIF1 expressing vectors. 9 clones resistant to SBI-756 were retrieved and DNA was extracted, transformed into TOP10 competent bacteria. Plasmids present in each clone were sequenced. All clones presented deletion or mutation of the helicase C-terminal domain. Stars indicate the presence of a stop codon. Q: Q motif, D: DEAD box. Bottom, TIF4631 deletions promote KY775 *S. cerevisiae* (pdr5D::hisG erg6D::hisG) strain resistance to SBI-756. KY775 cells were transformed with a library of randomly mutated TIF4631 expressing vectors. 12 clones resistant to SBI-756 were retrieved and DNA was extracted, transformed into TOP10 competent bacteria. Plasmids present in each clone were sequenced. All clones presented deletion of the C-terminal domains of TIF4631. Stars indicate the presence of a stop codon. MIF4G: middle domain of eukaryotic initiation factor 4G. (d) gRNA-235, gRNA-622 and EV A375 cells were seeded in 96 well plates. Cell proliferation was measured daily for 4 days using CellTiter-Glo.

Supplementary Figure 2. Characterize MA3 domain bound small molecules selected from In Silico screen.

(a) Testing funnel of high-throughput screening campaign (details in Methods). (b) Indicated melanoma and prostate cancer cell lines were treated with the four selected compounds, followed by viability assay after 72h. (c) EV and gRNA-235 A375 cells were treated with M19, followed by viability assay. (d) A375 cells were cultured in a medium containing indicated concentrations of FBS, followed by treatment with M19. Cell viability was measured 72 h later.

Supplementary Figure 3. RNAseq analysis of A375 cells treated with M19.

(a) Gene set enrichment analysis of RNAseq data of A375 cells treated with M19 (20 µM). The top enrichment plots of indicated pathways and corresponding heatmaps of up-regulated genes are shown. (b) IPA analysis of RNAseq data of A375 cells treated with M19 (20 µM); top activated pathways are shown (c) qPCR validation of selected differentially expressed genes. (d) representative genes and related signaling that were downregulated upon M19 treatment (left panel) and their validation by qPCR (right panel).

Supplementary Figure 4. Characterization of M19 analogs.

(a) A375 melanoma and H3A melanocyte cells were treated with indicated M19 analogs. Cell viability was measured 72 h later. (b) A375 cells (300 cells/well) were seeded in 12-well plates

and treated with indicated compounds. After one week, cells were stained with crystal violet. (c) A375 cells were treated with indicated concentrations of M19-6. qPCR analysis was performed on select differentially expressed genes. (d) A375 cells were pre-incubated with indicated concentrations of M19-6 for 2 h, followed by incubation with 3 µg/mL puromycin for 0.5 h. Cells were collected, lysed, and subjected to Western blot analysis using anti-puromycin antibody. The density of the whole lane was quantified by ImageJ and normalized to actin levels as indicated. (e) A375 cells were seeded in 384-well plate and treated with M19-6 after 24 h. The compound was removed from respective wells at indicated time points. Cell viability was measured 72h after the treatment. (f) Indicated BRAF mutant melanoma cells and spheroids were treated with M19-6, and cell viability was measured after 72 h for cell cultures and 96 h for spheroids. (g) Ten different NRas mutant melanoma cell lines were seeded in 384-well plates and treated with indicated concentrations of M19-6. Cell viability was measured after 72 h. (h,i) analyses of HDAC inhibitors with M19-6. A375 cells were seeded in 384-well plates and 24h later, M19-6 and Chidamide (H) or CI-994 (I) were added to respective wells at the indicated concentrations. Cell viability was measured after 72h using CellTiter-Glo.

Supplementary Figure 5. Characterization of ribosome footprints

(a) Distribution of read lengths for ribosome footprints generated using MNase digestion. (b) Stacked bar charts showing the proportion of reads from RNA-Seq and Ribo-Seq libraries mapped to different mRNA regions: coding sequence (CDS), 5' untranslated region (5' UTR), and 3' untranslated region (3' UTR). (c) Metagene analysis of ribosome profiling libraries generated by MNase, with reads from all mRNAs aligned within ±300 nucleotides of the start and stop codons.

Supplementary Figure 6. Characterization of anti-tumor immunity in vivo

(a) YUMM1.5 melanoma cells were inoculated into 8 weeks old C57BL/6 mice, and a week later subjected to M19-6 and its combination with FK228 (M19-6 + FK228) (n=5). Shown is tumor size and weight. (b,c) Quantification of tumor and lymph nodes infiltration of immune cells ($CD8^+$ T cells, $CD4^+$ T cells, NK1, DCs and macrophages) 12 days after tumor inoculation of YUMM1.5 cells into C57BL/6J mice that were treated with M19-6 or vehicle (n=7 mice per treatment). (d) Staining with CD8, FOXP3 and NK1 antibodies of tumors from C57BL/6J mice inoculated with YUMM1.5 cells and treated with M19-6 plus FK228. (n=3 mice per treatment). (e) RT-qPCR analysis of genes associated to activation of anti-tumor immunity from tumors from C57BL/6J mice inoculated with YUMM1.5 cells and treated with M19-6 plus FK228; and CH3 mice inoculated with SW1 cells and treated with M19-6. (n=3 mice per treatment).

References Cited

1. Livingstone A, Agarwal A, Stockler MR, Menzies AM, Howard K, Morton RL. Preferences for Immunotherapy in Melanoma: A Systematic Review. Ann Surg Oncol. 2020;27(2):571-84.
2. Weiss SA, Wolchok JD, Sznol M. Immunotherapy of Melanoma: Facts and Hopes. Clin Cancer Res. 2019;25(17):5191-201.
3. Flaherty KT. Targeting metastatic melanoma. Annu Rev Med. 2012;63:171-83.
4. Tsao H, Chin L, Garraway LA, Fisher DE. Melanoma: from mutations to medicine. Genes Dev. 2012;26(11):1131-55.
5. Singh K, Lin J, Lecomte N, Mohan P, Gokce A, Sanghvi VR, et al. Targeting eIF4A-Dependent Translation of KRAS Signaling Molecules. Cancer Res. 2021;81(8):2002-14.
6. Biswas B, Guemiri R, Cadix M, Labbe CM, Chakraborty A, Dutertre M, et al. Differential Effects on the Translation of Immune-Related Alternatively Polyadenylated mRNAs in Melanoma and T Cells by eIF4A Inhibition. Cancers (Basel). 2022;14(5).
7. Boussemart L, Malka-Mahieu H, Girault I, Allard D, Hemmingsson O, Tomasic G, et al. eIF4F is a nexus of resistance to anti-BRAF and anti-MEK cancer therapies. Nature. 2014;513(7516):105-9.
8. Feng Y, Pinkerton AB, Hulea L, Zhang T, Davies MA, Grotegut S, et al. SBI-0640756 Attenuates the Growth of Clinically Unresponsive Melanomas by Disrupting the eIF4F Translation Initiation Complex. Cancer Res. 2015;75(24):5211-8.
9. Pelletier J, Sonenberg N. The Organizing Principles of Eukaryotic Ribosome Recruitment. Annu Rev Biochem. 2019;88:307-35.
10. Silvera D, Formenti SC, Schneider RJ. Translational control in cancer. Nat Rev Cancer. 2010;10(4):254-66.
11. Sonenberg N, Dever TE. Eukaryotic translation initiation factors and regulators. Curr Opin Struct Biol. 2003;13(1):56-63.
12. Chu J, Cargnello M, Topisirovic I, Pelletier J. Translation Initiation Factors: Reprogramming Protein Synthesis in Cancer. Trends Cell Biol. 2016;26(12):918-33.
13. Bhat M, Robichaud N, Hulea L, Sonenberg N, Pelletier J, Topisirovic I. Targeting the translation machinery in cancer. Nat Rev Drug Discov. 2015;14(4):261-78.
14. Alain T, Morita M, Fonseca BD, Yanagiya A, Siddiqui N, Bhat M, et al. eIF4E/4E-BP ratio predicts the efficacy of mTOR targeted therapies. Cancer Res. 2012;72(24):6468-76.
15. Robichaud N, Sonenberg N, Ruggero D, Schneider RJ. Translational Control in Cancer. Cold Spring Harb Perspect Biol. 2019;11(7).
16. Kovalski JR, Kuzuoglu-Ozturk D, Ruggero D. Protein synthesis control in cancer: selectivity and therapeutic targeting. EMBO J. 2022;41(8):e109823.
17. Chu J, Pelletier J. Targeting the eIF4A RNA helicase as an anti-neoplastic approach. Biochimica Et Biophysica Acta-Gene Regulatory Mechanisms. 2015;1849(7):781-91.
18. Herzog LO, Walters B, Buono R, Lee JS, Mallya S, Fung A, et al. Targeting eIF4F translation initiation complex with SBI-756 sensitises B lymphoma cells to venetoclax. Br J Cancer. 2021;124(6):1098-109.
19. Khosravi S, Tam KJ, Ardekani GS, Martinka M, McElwee KJ, Ong CJ. eIF4E Is an Adverse Prognostic Marker of Melanoma Patient Survival by Increasing Melanoma Cell Invasion. Journal of Investigative Dermatology. 2015;135(5):1358-67.
20. Joyce CE, Yanez AG, Mori A, Yoda A, Carroll JS, Novina CD. Differential Regulation of the Melanoma Proteome by eIF4A1 and eIF4E. Cancer Res. 2017;77(3):613-22.
21. Badura M, Braunstein S, Zavadil J, Schneider RJ. DNA damage and eIF4G1 in breast cancer cells reprogram translation for survival and DNA repair mRNAs. Proc Natl Acad Sci U S A. 2012;109(46):18767-72.

22. Del Valle L, Dai L, Lin HY, Lin Z, Chen J, Post SR, et al. Role of EIF4G1 network in non-small cell lung cancers (NSCLC) cell survival and disease progression. J Cell Mol Med. 2021;25(6):2795-805.
23. Silvera D, Arju R, Darvishian F, Levine PH, Zolfaghari L, Goldberg J, et al. Essential role for eIF4GI overexpression in the pathogenesis of inflammatory breast cancer. Nat Cell Biol. 2009;11(7):903-8.
24. Ramirez-Valle F, Braunstein S, Zavadil J, Formenti SC, Schneider RJ. eIF4GI links nutrient sensing by mTOR to cell proliferation and inhibition of autophagy. J Cell Biol. 2008;181(2):293-307.
25. Fukuchi-Shimogori T, Ishii I, Kashiwagi K, Mashiba H, Ekimoto H, Igarashi K. Malignant transformation by overproduction of translation initiation factor eIF4G. Cancer Res. 1997;57(22):5041-4.
26. Bitterman PB, Polunovsky VA. Attacking a nexus of the oncogenic circuitry by reversing aberrant eIF4F-mediated translation. Mol Cancer Ther. 2012;11(5):1051-61.
27. Ramon YCS, Castellvi J, Hummer S, Peg V, Pelletier J, Sonenberg N. Beyond molecular tumor heterogeneity: protein synthesis takes control. Oncogene. 2018;37(19):2490-501.
28. Malka-Mahieu H, Girault I, Rubington M, Leriche M, Welsch C, Kamsu-Kom N, et al. Synergistic effects of eIF4A and MEK inhibitors on proliferation of NRAS-mutant melanoma cell lines. Cell Cycle. 2016;15(18):2405-9.
29. Hashimoto A, Handa H, Hata S, Tsutaho A, Yoshida T, Hirano S, et al. Inhibition of mutant KRAS-driven overexpression of ARF6 and MYC by an eIF4A inhibitor drug improves the effects of anti-PD-1 immunotherapy for pancreatic cancer. Cell Commun Signal. 2021;19(1):54.
30. Gerson-Gurwitz A, Young NP, Goel VK, Eam B, Stumpf CR, Chen J, et al. Zotatifin, an eIF4A-Selective Inhibitor, Blocks Tumor Growth in Receptor Tyrosine Kinase Driven Tumors. Front Oncol. 2021;11:766298.
31. Zhao N, Kabotyanski EB, Saltzman AB, Malovannaya A, Yuan X, Reineke LC, et al. Targeting eIF4A triggers an interferon response to synergize with chemotherapy and suppress triple-negative breast cancer. J Clin Invest. 2023;133(24).
32. Nardi F, Perurena N, Schade AE, Li ZH, Ngo K, Ivanova EV, et al. Cotargeting a MYC/eIF4A-survival axis improves the efficacy of KRAS inhibitors in lung cancer. J Clin Invest. 2023;133(16).
33. Cencic R, Im YK, Naineni SK, Moustafa-Kamal M, Jovanovic P, Sabourin V, et al. A second-generation eIF4A RNA helicase inhibitor exploits translational reprogramming as a vulnerability in triple-negative breast cancer. Proc Natl Acad Sci U S A. 2024;121(4):e2318093121.
34. Feng Y, Lau E, Scortegagna M, Ruller C, De SK, Barile E, et al. Inhibition of melanoma development in the Nras((Q61K)) ::Ink4a(-/-) mouse model by the small molecule BI-69A11. Pigment Cell Melanoma Res. 2013;26(1):136-42.
35. He L, Zhang X, Shi F, Zhang H, Chen Y, Sun K, et al. Reprograming immunosuppressive microenvironment by eIF4G1 targeting to eradicate pancreatic ductal adenocarcinoma. Cell Rep Med. 2024;5(10):101731.
36. Levy-Strumpf N, Kimchi A. Death associated proteins (DAPs): from gene identification to the analysis of their apoptotic and tumor suppressive functions. Oncogene. 1998;17(25):3331-40.
37. Loh PG, Yang HS, Walsh MA, Wang Q, Wang X, Cheng Z, et al. Structural basis for translational inhibition by the tumour suppressor Pdcd4. EMBO J. 2009;28(3):274-85.
38. Waters LC, Strong SL, Ferlemann E, Oka O, Muskett FW, Veverka V, et al. Structure of the tandem MA-3 region of Pdcd4 protein and characterization of its interactions with eIF4A and eIF4G: molecular mechanisms of a tumor suppressor. J Biol Chem. 2011;286(19):17270-80.
39. Suzuki C, Garces RG, Edmonds KA, Hiller S, Hyberts SG, Marintchev A, et al. PDCD4 inhibits translation initiation by binding to eIF4A using both its MA3 domains. Proc Natl Acad Sci U S A. 2008;105(9):3274-9.
40. Waters LC, Veverka V, Bohm M, Schmedt T, Choong PT, Muskett FW, et al. Structure of the C-terminal MA-3 domain of the tumour suppressor protein Pdcd4 and characterization of its interaction with eIF4A. Oncogene. 2007;26(34):4941-50.

41. Ingolia NT, Ghaemmaghami S, Newman JR, Weissman JS. Genome-wide analysis in vivo of translation with nucleotide resolution using ribosome profiling. Science. 2009;324(5924):218-23.
42. Gandin V, Sikstrom K, Alain T, Morita M, McLaughlan S, Larsson O, et al. Polysome fractionation and analysis of mammalian translatomes on a genome-wide scale. J Vis Exp. 2014(87).
43. Phillips SE. Turning up the HEAT on translation. Structure. 2006;14(5):806-7.
44. Bhachoo J, Beuming T. Investigating Protein-Peptide Interactions Using the Schrodinger Computational Suite. Methods Mol Biol. 2017;1561:235-54.
45. Ban F, Dalal K, Li H, LeBlanc E, Rennie PS, Cherkasov A. Best Practices of Computer-Aided Drug Discovery: Lessons Learned from the Development of a Preclinical Candidate for Prostate Cancer with a New Mechanism of Action. J Chem Inf Model. 2017;57(5):1018-28.
46. Chothani S, Adami E, Ouyang JF, Viswanathan S, Hubner N, Cook SA, et al. deltaTE: Detection of Translationally Regulated Genes by Integrative Analysis of Ribo-seq and RNA-seq Data. Curr Protoc Mol Biol. 2019;129(1):e108.
47. Love MI, Huber W, Anders S. Moderated estimation of fold change and dispersion for RNA-seq data with DESeq2. Genome Biol. 2014;15(12):550.
48. Jain V, Singh MP, Amaravadi RK. Recent advances in targeting autophagy in cancer. Trends Pharmacol Sci. 2023;44(5):290-302.
49. Price JE, Tarin D, Fidler IJ. Influence of organ microenvironment on pigmentation of a metastatic murine melanoma. Cancer Res. 1988;48(8):2258-64.
50. Bhoumik A, Gangi L, Ronai Z. Inhibition of melanoma growth and metastasis by ATF2-derived peptides. Cancer Res. 2004;64(22):8222-30.
51. Qi J, Nakayama K, Gaitonde S, Goydos JS, Krajewski S, Eroshkin A, et al. The ubiquitin ligase Siah2 regulates tumorigenesis and metastasis by HIF-dependent and -independent pathways. Proc Natl Acad Sci U S A. 2008;105(43):16713-8.
52. Tacar O, Sriamornsak P, Dass CR. Doxorubicin: an update on anticancer molecular action, toxicity and novel drug delivery systems. J Pharm Pharmacol. 2013;65(2):157-70.
53. Scortegagna M, Murad R, Bina P, Feng Y, Porritt RA, Terskikh AV, et al. Age-Associated Modulation of TREM1/2-Expressing Macrophages Promotes Melanoma Progression and Metastasis. Cancer Res. 2025;85(12):2218-33.
54. Truitt ML, Conn CS, Shi Z, Pang X, Tokuyasu T, Coady AM, et al. Differential Requirements for eIF4E Dose in Normal Development and Cancer. Cell. 2015;162(1):59-71.
55. Ernst JT, Thompson PA, Nilewski C, Sprengeler PA, Sperry S, Packard G, et al. Design of Development Candidate eFT226, a First in Class Inhibitor of Eukaryotic Initiation Factor 4A RNA Helicase. J Med Chem. 2020;63(11):5879-955.
56. Lamphear BJ, Kirchweger R, Skern T, Rhoads RE. Mapping of functional domains in eukaryotic protein synthesis initiation factor 4G (eIF4G) with picornaviral proteases. Implications for cap-dependent and cap-independent translational initiation. J Biol Chem. 1995;270(37):21975-83.
57. Goel S, Bergholz JS, Zhao JJ. Targeting CDK4 and CDK6 in cancer. Nat Rev Cancer. 2022;22(6):356-72.
58. Doench JG, Fusi N, Sullender M, Hegde M, Vaimberg EW, Donovan KF, et al. Optimized sgRNA design to maximize activity and minimize off-target effects of CRISPR-Cas9. Nat Biotechnol. 2016;34(2):184-91.
59. Sanson KR, Hanna RE, Hegde M, Donovan KF, Strand C, Sullender ME, et al. Optimized libraries for CRISPR-Cas9 genetic screens with multiple modalities. Nat Commun. 2018;9(1):5416.
60. Kim HK, Min S, Song M, Jung S, Choi JW, Kim Y, et al. Deep learning improves prediction of CRISPR-Cpf1 guide RNA activity. Nat Biotechnol. 2018;36(3):239-41.

61. Canver MC, Haeussler M, Bauer DE, Orkin SH, Sanjana NE, Shalem O, et al. Integrated design, execution, and analysis of arrayed and pooled CRISPR genome-editing experiments. Nat Protoc. 2018;13(5):946-86.
62. Dobin A, Davis CA, Schlesinger F, Drenkow J, Zaleski C, Jha S, et al. STAR: ultrafast universal RNA-seq aligner. Bioinformatics. 2013;29(1):15-21.
63. Ramirez F, Ryan DP, Gruning B, Bhardwaj V, Kilpert F, Richter AS, et al. deepTools2: a next generation web server for deep-sequencing data analysis. Nucleic Acids Res. 2016;44(W1):W160-5.
64. Ewels P, Magnusson M, Lundin S, Kaller M. MultiQC: summarize analysis results for multiple tools and samples in a single report. Bioinformatics. 2016;32(19):3047-8.
65. Subramanian A, Tamayo P, Mootha VK, Mukherjee S, Ebert BL, Gillette MA, et al. Gene set enrichment analysis: a knowledge-based approach for interpreting genome-wide expression profiles. Proc Natl Acad Sci U S A. 2005;102(43):15545-50.
66. Friesner RA, Banks JL, Murphy RB, Halgren TA, Klicic JJ, Mainz DT, et al. Glide: a new approach for rapid, accurate docking and scoring. 1. Method and assessment of docking accuracy. J Med Chem. 2004;47(7):1739-49.
67. McGann M. FRED pose prediction and virtual screening accuracy. J Chem Inf Model. 2011;51(3):578-96.
68. Irwin JJ, Tang KG, Young J, Dandarchuluun C, Wong BR, Khurelbaatar M, et al. ZINC20-A Free Ultralarge-Scale Chemical Database for Ligand Discovery. J Chem Inf Model. 2020;60(12):6065-73.
69. Goodsell DS, Sanner MF, Olson AJ, Forli S. The AutoDock suite at 30. Protein Sci. 2021;30(1):31-43.
70. Eswar N, Eramian D, Webb B, Shen MY, Sali A. Protein structure modeling with MODELLER. Methods Mol Biol. 2008;426:145-59.
71. Morris GM, Huey R, Lindstrom W, Sanner MF, Belew RK, Goodsell DS, et al. AutoDock4 and AutoDockTools4: Automated docking with selective receptor flexibility. J Comput Chem. 2009;30(16):2785-91.
72. Oda A, Tsuchida K, Takakura T, Yamaotsu N, Hirono S. Comparison of consensus scoring strategies for evaluating computational models of protein-ligand complexes. J Chem Inf Model. 2006;46(1):380-91.
73. Daina A, Michielin O, Zoete V. SwissADME: a free web tool to evaluate pharmacokinetics, drug-likeness and medicinal chemistry friendliness of small molecules. Sci Rep. 2017;7:42717.
74. Gentile F, Agrawal V, Hsing M, Ton AT, Ban F, Norinder U, et al. Deep Docking: A Deep Learning Platform for Augmentation of Structure Based Drug Discovery. ACS Cent Sci. 2020;6(6):939-49.
75. Nettleton DO, Einolf HJ. Assessment of cytochrome p450 enzyme inhibition and inactivation in drug discovery and development. Curr Top Med Chem. 2011;11(4):382-403.
76. Lobo S. Is there enough focus on lipophilicity in drug discovery? Expert Opin Drug Discov. 2020;15(3):261-3.
77. Ingolia NT, Brar GA, Rouskin S, McGeachy AM, Weissman JS. The ribosome profiling strategy for monitoring translation in vivo by deep sequencing of ribosome-protected mRNA fragments. Nat Protoc. 2012;7(8):1534-50.
78. Langmead B, Trapnell C, Pop M, Salzberg SL. Ultrafast and memory-efficient alignment of short DNA sequences to the human genome. Genome Biol. 2009;10(3):R25.
79. Frankish A, Diekhans M, Ferreira AM, Johnson R, Jungreis I, Loveland J, et al. GENCODE reference annotation for the human and mouse genomes. Nucleic Acids Res. 2019;47(D1):D766-D73.
80. Smith T, Heger A, Sudbery I. UMI-tools: modeling sequencing errors in Unique Molecular Identifiers to improve quantification accuracy. Genome Res. 2017;27(3):491-9.
81. Kiniry SJ, Judge CE, Michel AM, Baranov PV. Trips-Viz: an environment for the analysis of public and user-generated ribosome profiling data. Nucleic Acids Res. 2021;49(W1):W662-W70.

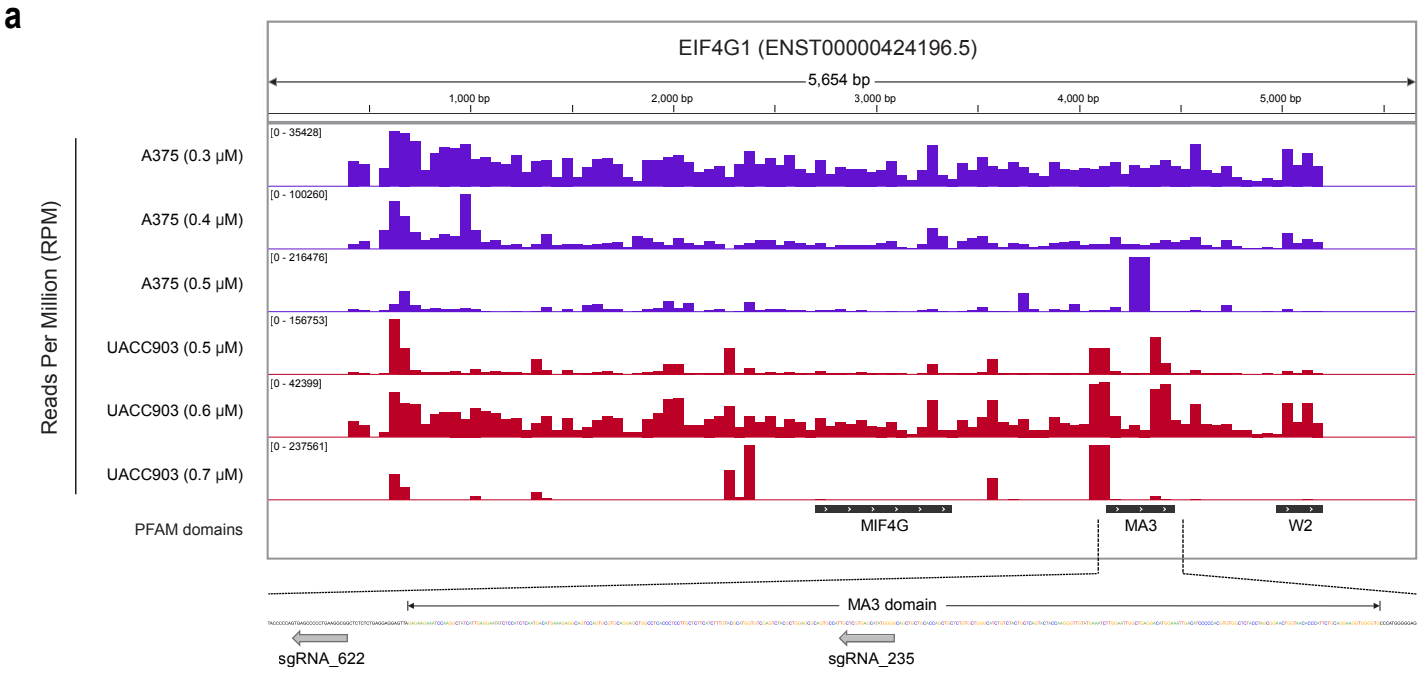
a
EIF4G1 (ENST00000424196.5)
5,654 bp
1,000 bp
2,000 bp
3,000 bp
4,000 bp
5,000 bp
Reads Per Million (RPM)
A375 (0.3 μM)
A375 (0.4 μM)
A375 (0.5 μM)
UACC903 (0.5 μM)
UACC903 (0.6 μM)
UACC903 (0.7 μM)
[0 - 35428]
[0 - 100260]
[0 - 216476]
[0 - 156753]
[0 - 42399]
[0 - 237561]
PFAM domains
MIF4G
MA3
W2
MA3 domain
sgRNA_622
sgRNA_235

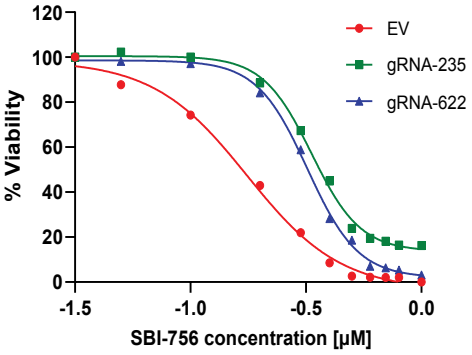
b
% Viability
SBI-756 concentration [μM]
EV
gRNA-235
gRNA-622

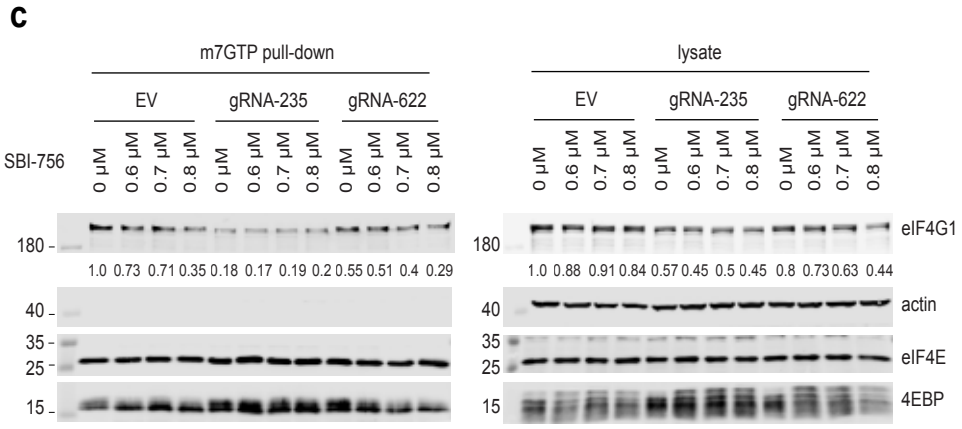
c
m7GTP pull-down
lysate
EV
gRNA-235
gRNA-622
SBI-756
0 μM
0.6 μM
0.7 μM
0.8 μM
eIF4G1
actin
eIF4E
4EBP
1.0 0.73 0.71 0.35 0.18 0.17 0.19 0.2 0.55 0.51 0.4 0.29
1.0 0.88 0.91 0.84 0.57 0.45 0.5 0.45 0.8 0.73 0.63 0.44

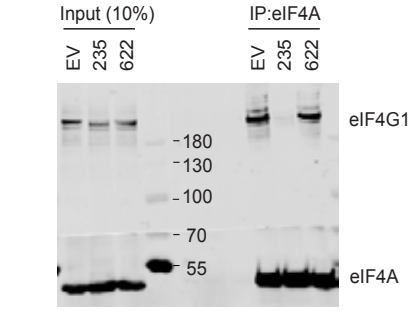
d
Input (10%)
IP:eIF4A
EV
235
622
eIF4G1
eIF4A
180
130
100
70
55

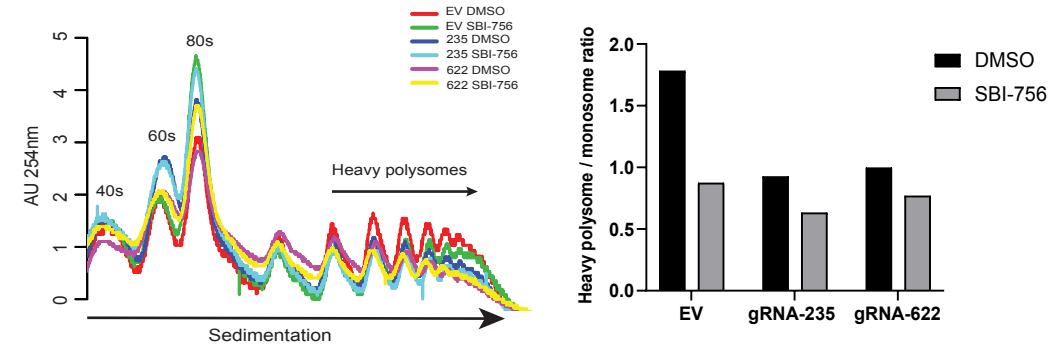
e
EV DMSO
EV SBI-756
235 DMSO
235 SBI-756
622 DMSO
622 SBI-756
AU 254nm
40s
60s
80s
Heavy polysomes
Sedimentation
Heavy polysome / monosome ratio
DMSO
SBI-756
EV
gRNA-235
gRNA-622

a

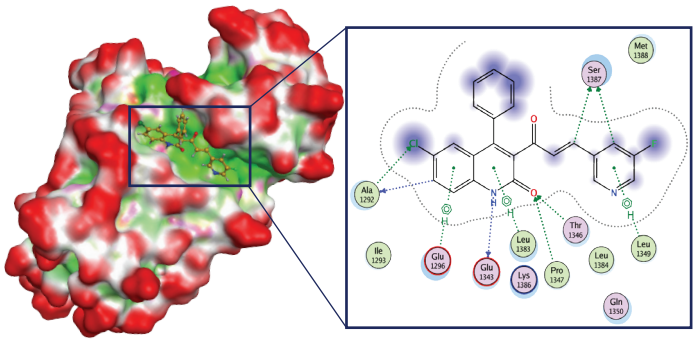
Met 1388
Ser 1387
Ala 1292
Thr 1346
Leu 1383
Leu 1349
Ile 1291
Glu 1296
Glu 1341
Lys 1386
Pro 1347
Leu 1384
Gln 1350

b

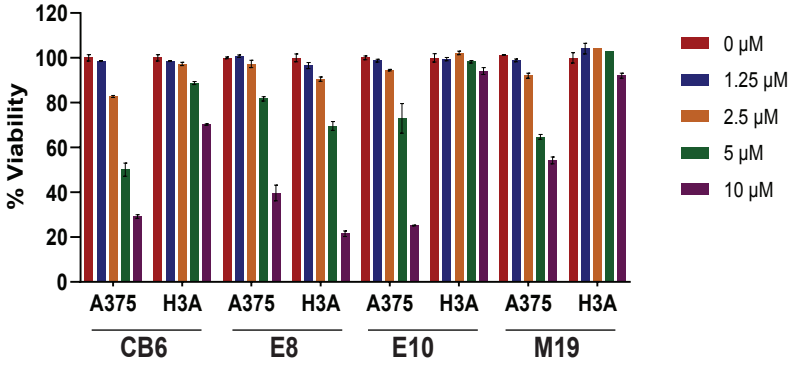
% Viability
120
100
80
60
40
20
0
A375
H3A
A375
H3A
A375
H3A
A375
H3A
CB6
E8
E10
M19
0 μM
1.25 μM
2.5 μM
5 μM
10 μM

c

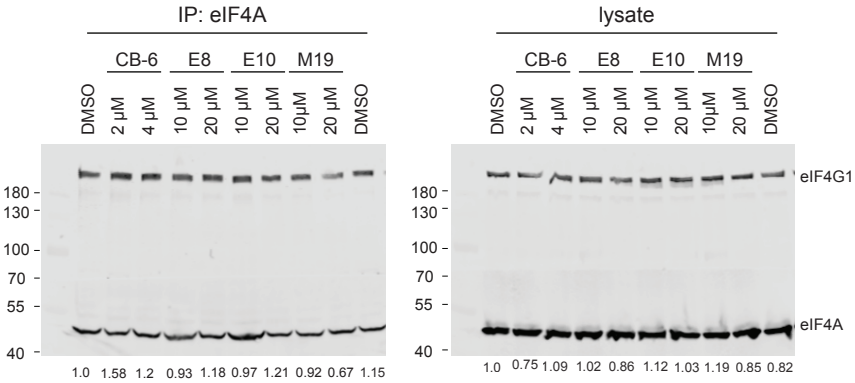
IP: eIF4A
lysate
CB-6
E8
E10
M19
DMSO
2 μM
4 μM
10 μM
20 μM
10 μM
20 μM
10μM
20 μM
DMSO
180
130
100
70
55
40
eIF4G1
eIF4A
1.0 1.58 1.2 0.93 1.18 0.97 1.21 0.92 0.67 1.15
1.0 0.75 1.09 1.02 0.86 1.12 1.03 1.19 0.85 0.82

d

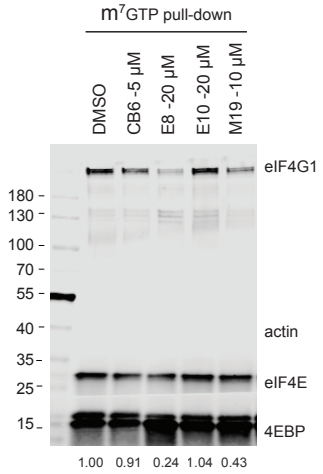
m7GTP pull-down
DMSO
CB6 -5 μM
E8 -20 μM
E10 -20 μM
M19 -10 μM
180
130
100
70
55
40
35
25
15
eIF4G1
actin
eIF4E
4EBP
1.00 0.91 0.24 1.04 0.43

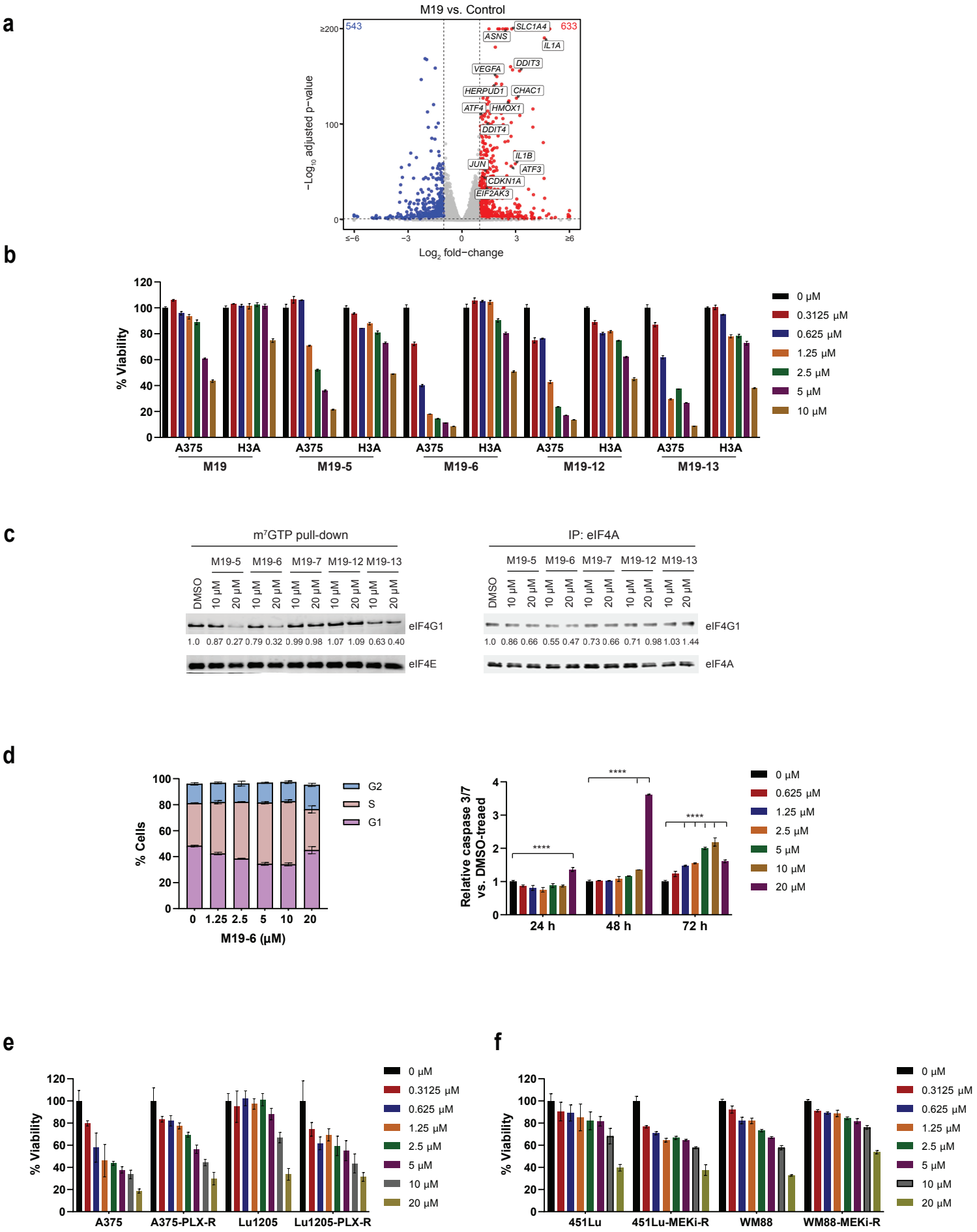

Feng, Olea et al. Fig. 3

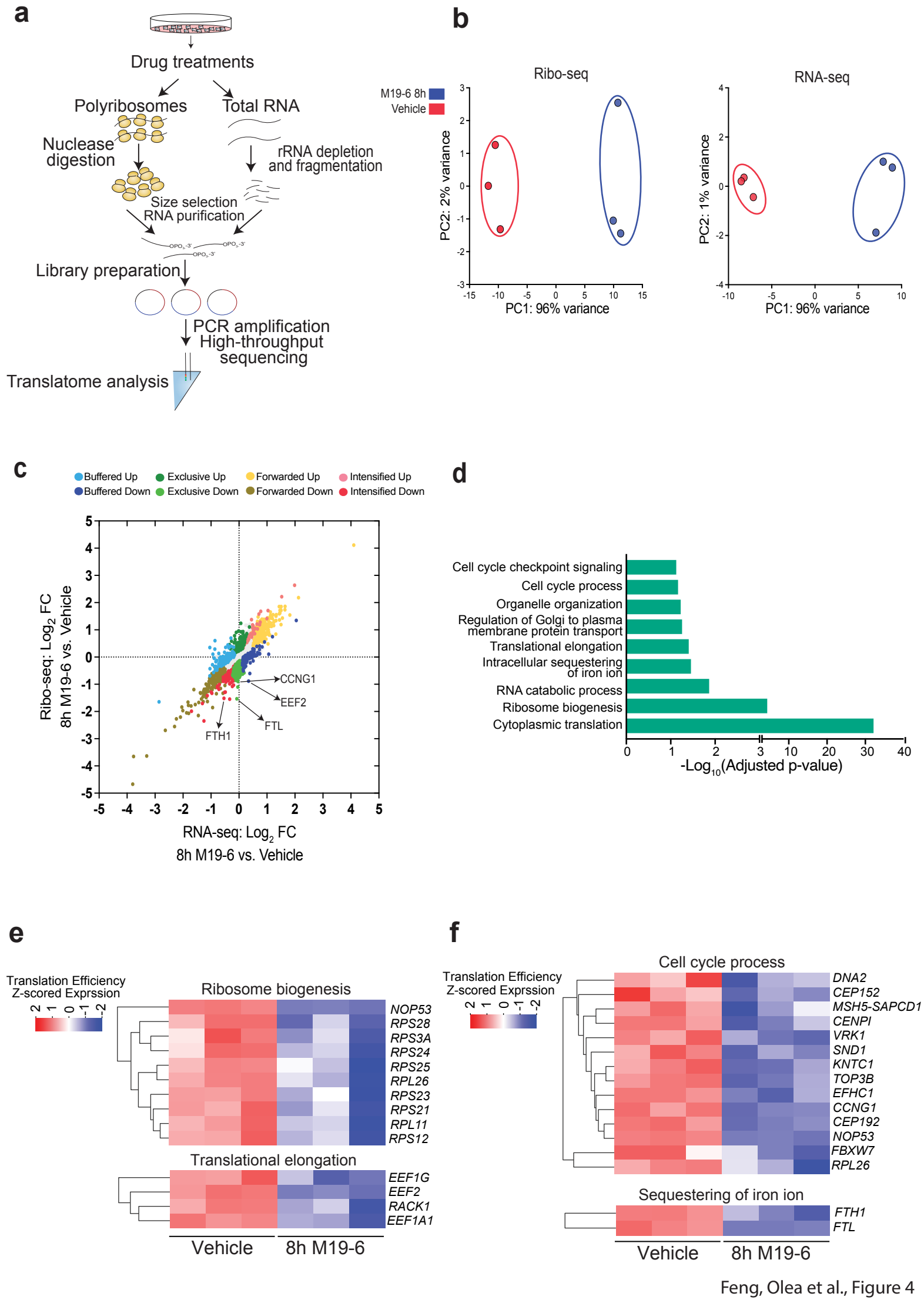

Feng, Olea et al., Figure 4

a

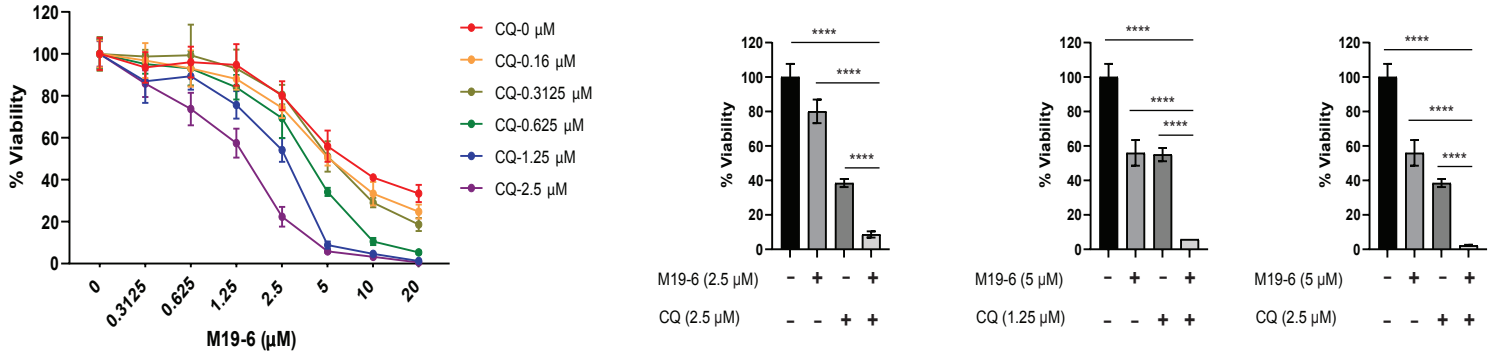
% Viability
M19-6 (μM)
CQ-0 μM
CQ-0.16 μM
CQ-0.3125 μM
CQ-0.625 μM
CQ-1.25 μM
CQ-2.5 μM
M19-6 (2.5 μM)
CQ (2.5 μM)
M19-6 (5 μM)
CQ (1.25 μM)
CQ (2.5 μM)
****

b

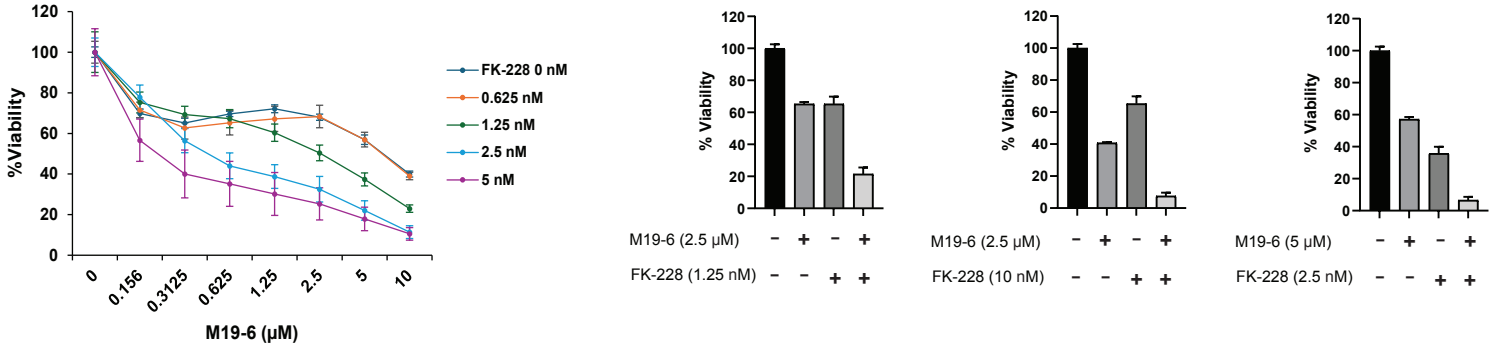
%Viability
M19-6 (μM)
FK-228 0 nM
0.625 nM
1.25 nM
2.5 nM
5 nM
% Viability
M19-6 (2.5 μM)
FK-228 (1.25 nM)
FK-228 (10 nM)
M19-6 (5 μM)
FK-228 (2.5 nM)

c

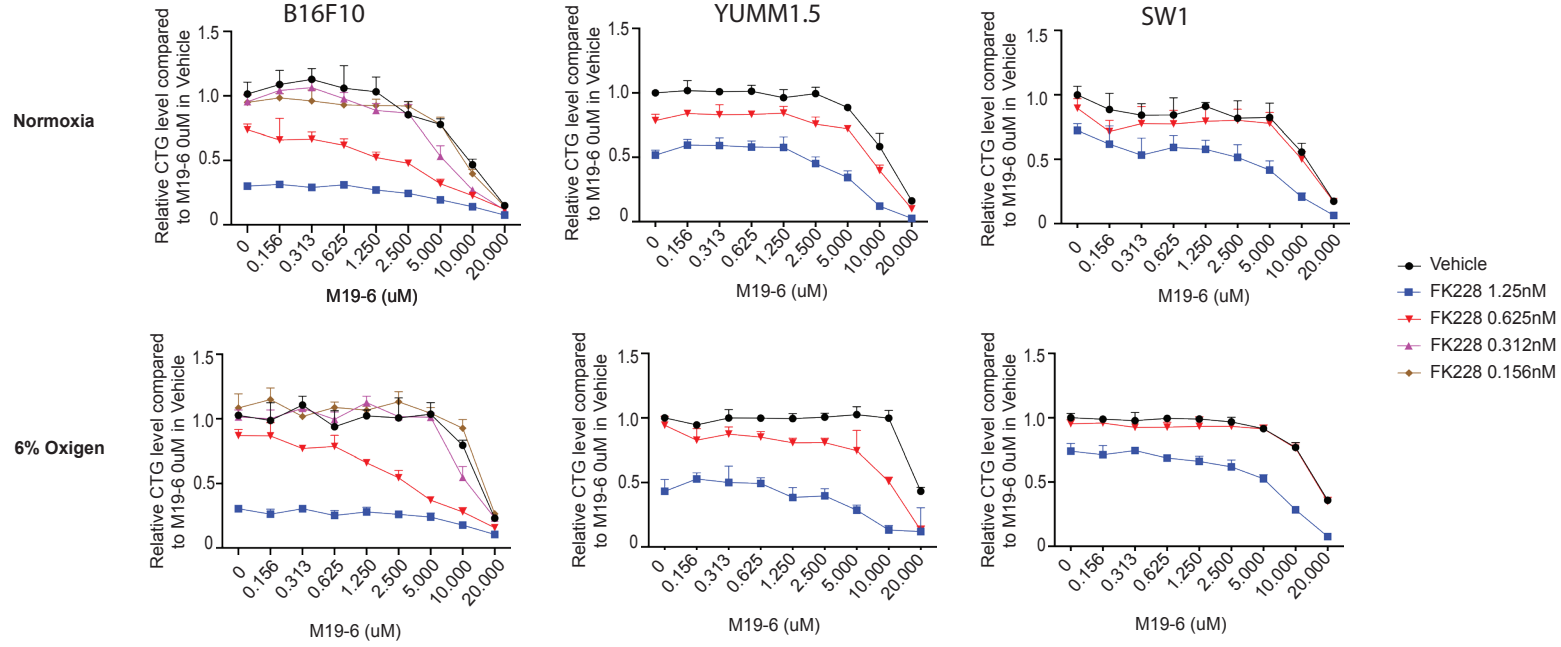
Normoxia
6% Oxigen
B16F10
YUMM1.5
SW1
Relative CTG level compared to M19-6 0uM in Vehicle
M19-6 (uM)
Vehicle
FK228 1.25nM
FK228 0.625nM
FK228 0.312nM
FK228 0.156nM

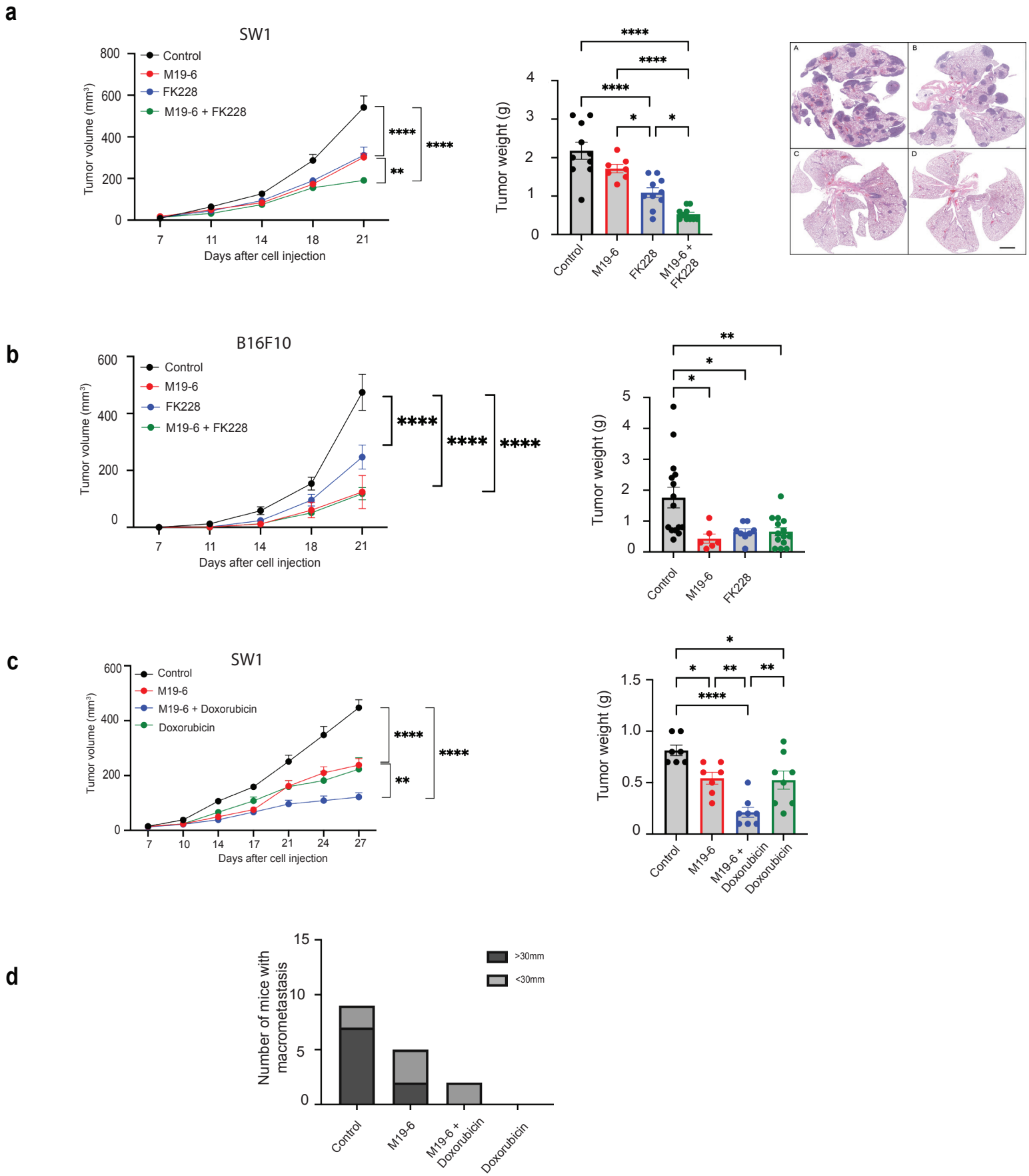

Feng, Olea et al., Figure 6

a

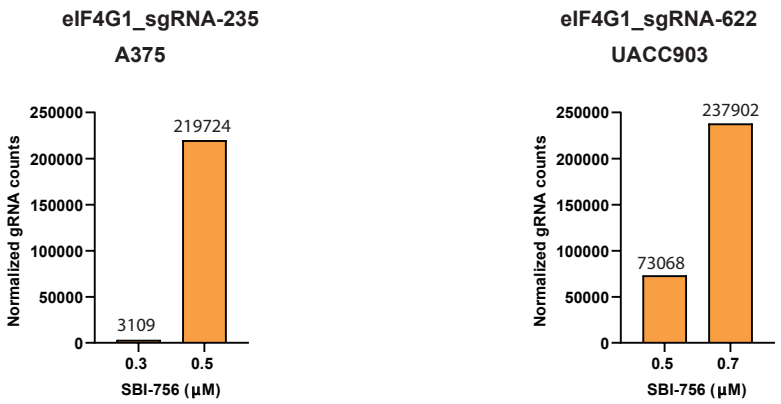

b

GAGAAGAAATCCAAGGCTATCATTGAGGAATATCTCCATCTCAATGACATGAAAGAGGCAGTCCAGTGCGTGCAGGAGCTGGCCTCA
CCCTCCTTGCTCTTCATCTTTGTACGGCATGGTGTCGAGTCTACGCTGGAGCGCAGTGCC**ATTGCTCGTGAGCATATGGGG**CAGCTG
CTGCACCAGCTGCTCTGTGCTGGGCATCTGTCTACTGCTCAGTACTACCAAGGGTTGTATGAAATCTTGGAATTGGCTGAGGACATGG
AAATTGACATCCCCCACGTGTGGCTCTACCTAGCGGAACTGGTAACACCCATTCTGCAGGAA~~GGTGGGGTG~~

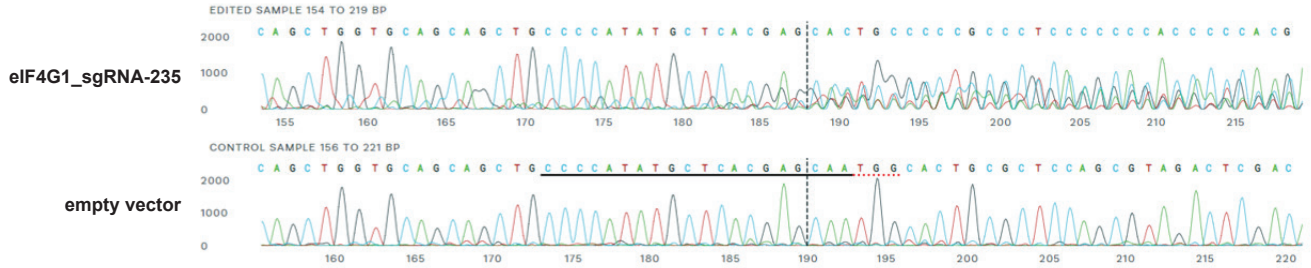

TGCGCAAGGCAGCTAGCCTCACGGAGGATCGGGACCGTGGGCGGGATGCCGTGAAGCGAGAAGCTGCCCTACCCC**CAGTGAGCCCCCTGAAGGCG**GCT
CTCTCTGAGGAGGAGTTAGAGAAGAAATCCAAGGCTATCATTGAGGAATATCTCCATCTCAATGACATGAAAGAGGCAGTCCAGTGCGTG
CAGGAGCTGGCCTCACCCTCCTTGCTCTTCATCTTTGTACGGCATGGTGTCGAGTCTACGCTGGAGCGCAGTGCCATTGCTCGTGAG
CATATGGGGCAGCTGCTGCACCAGCTGCTCTGTGCTGGGCATCTGTCTACTGCTCAGTACTACCAAG~~GGGTTGTATGAA~~ATCTTGG AAT
TGGCTGAGGACATGGAAATTGACATCCCCCACGTGTGGCTCTACCTAGCGGAACTGGTAACACCCATTCTGCAGGAAGGTGGGGTG

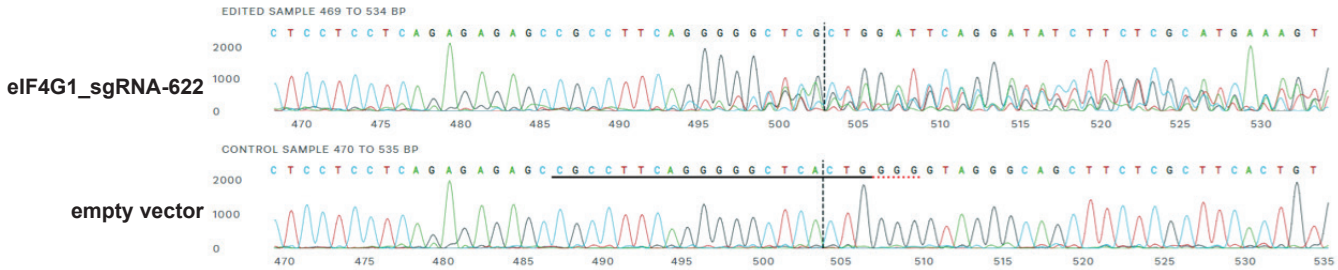

c

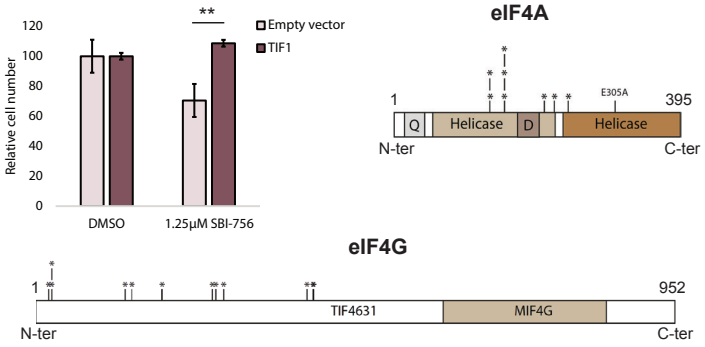

d

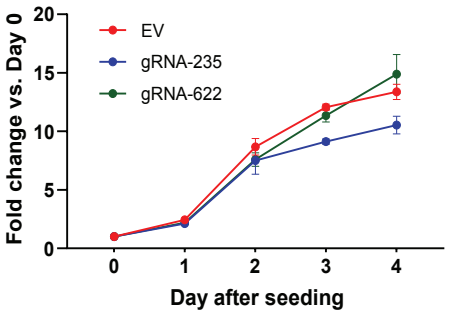

a

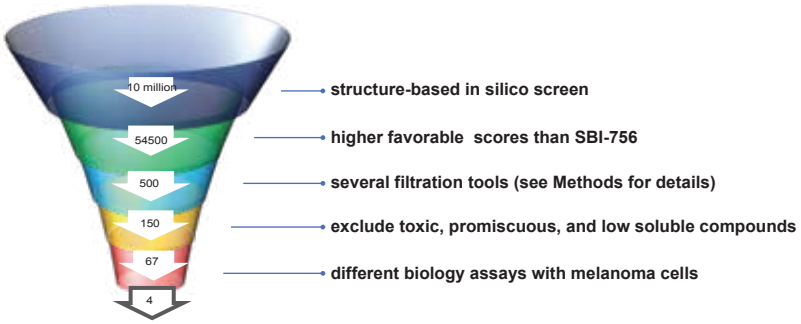
10 million
54500
500
150
67
4
structure-based in silico screen
higher favorable scores than SBI-756
several filtration tools (see Methods for details)
exclude toxic, promiscuous, and low soluble compounds
different biology assays with melanoma cells

b

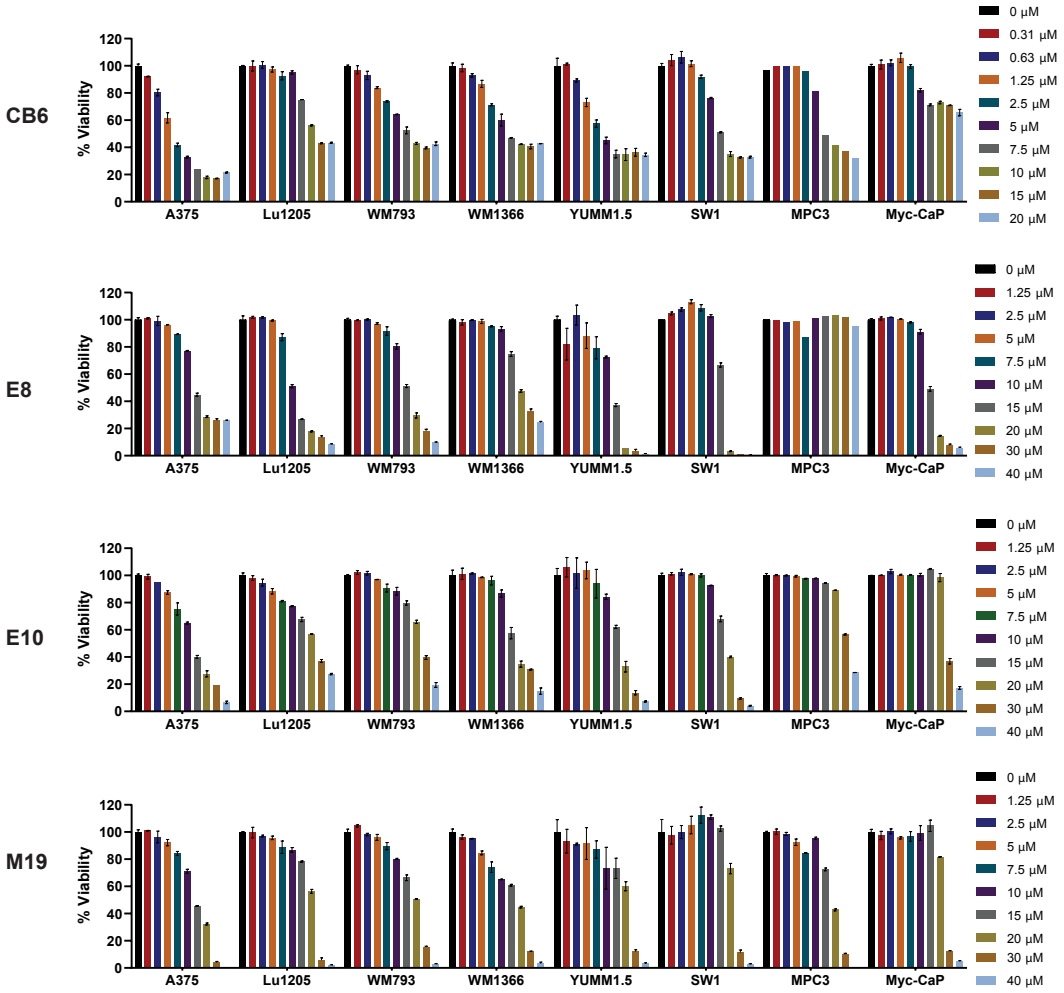
CB6
E8
E10
M19
% Viability
A375
Lu1205
WM793
WM1366
YUMM1.5
SW1
MPC3
Myc-CaP
0 μM
0.31 μM
0.63 μM
1.25 μM
2.5 μM
5 μM
7.5 μM
10 μM
15 μM
20 μM
30 μM
40 μM

c

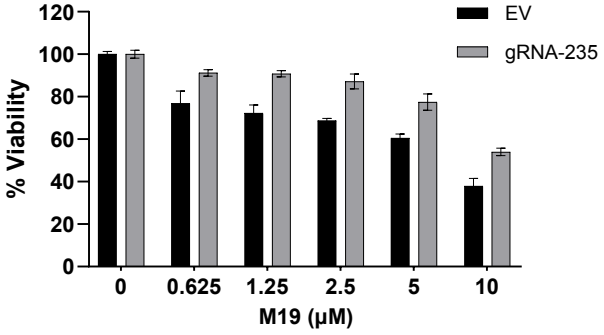
% Viability
EV
gRNA-235
0
0.625
1.25
2.5
5
10
M19 (μM)

d

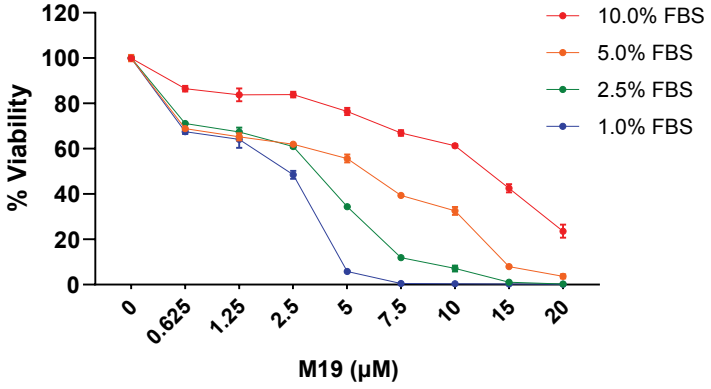
% Viability
10.0% FBS
5.0% FBS
2.5% FBS
1.0% FBS
0
0.625
1.25
2.5
5
7.5
10
15
20
M19 (μM)

a

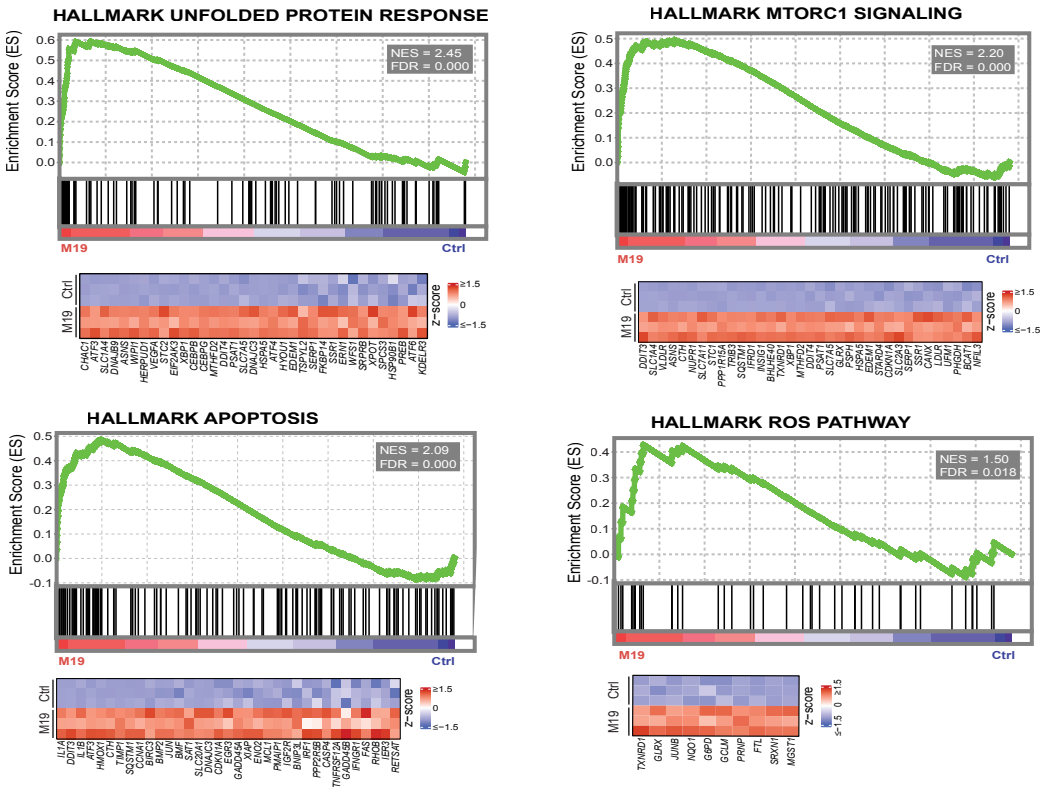

b

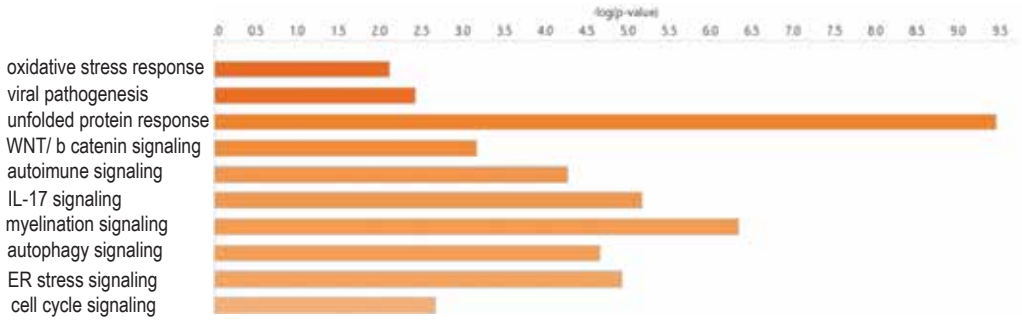

c

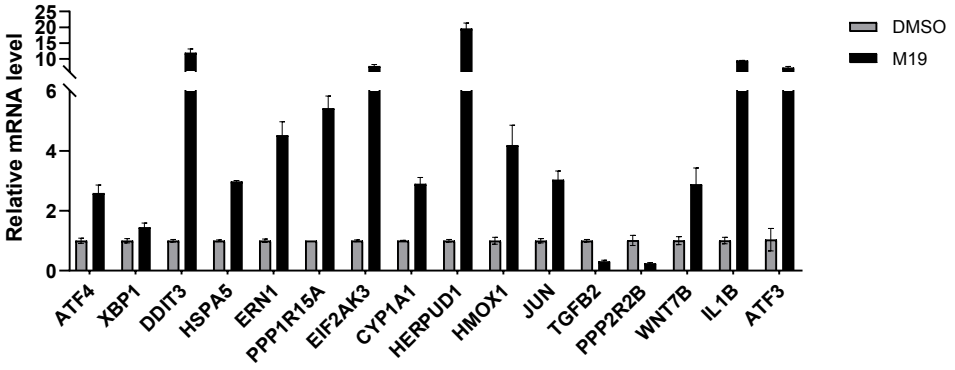

d

Top E2F targets genes

SYMBOL	RANK METRIC SCORE
CDKN2C	-2.328
E2F8	-2.262
CDKN3	-1.901
UNG	-1.809
BIRC5	-1.797
SPC25	-1.788
MCM6	-1.786
PCNA	-1.769
SPC24	-1.728
LMNB1	-1.694

Top G2M target genes

SYMBOL	RANK METRIC SCORE
CDKN2C	-2.328
E2F2	-2.177
CDKN3	-1.901
GINS2	-1.835
BIRC5	-1.797
MCM6	-1.786
LMNB1	-1.694
CCNF	-1.651
TOP2A	-1.646
HMMR	-1.607

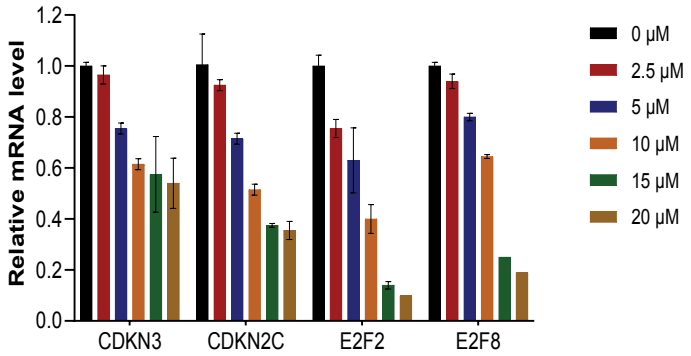

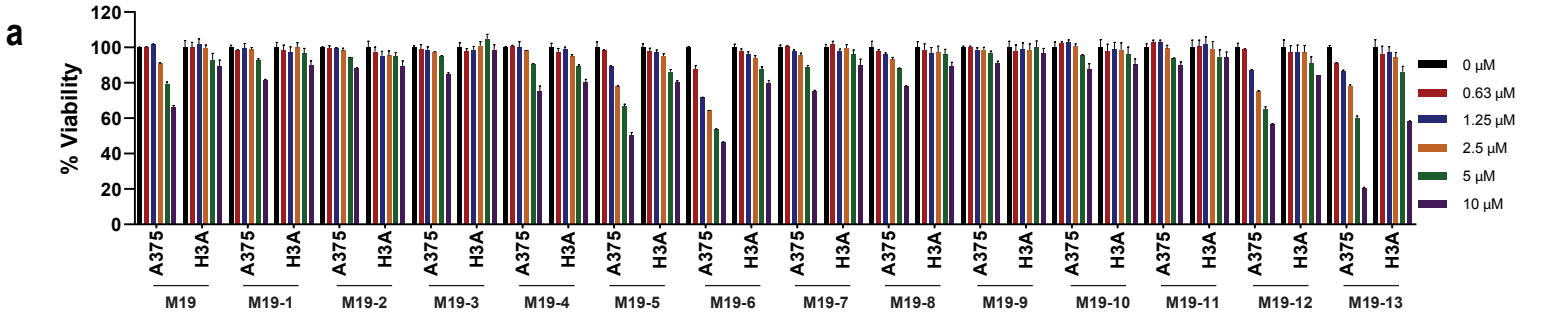

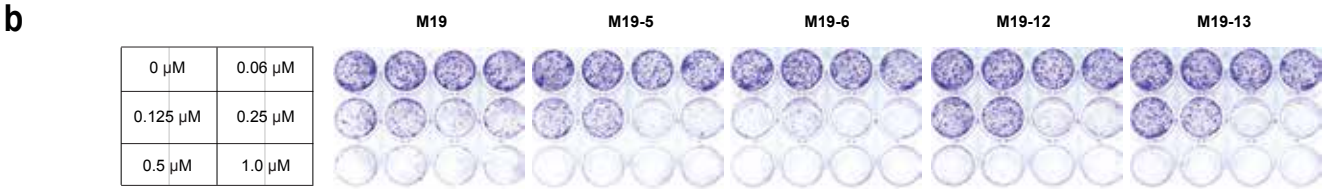

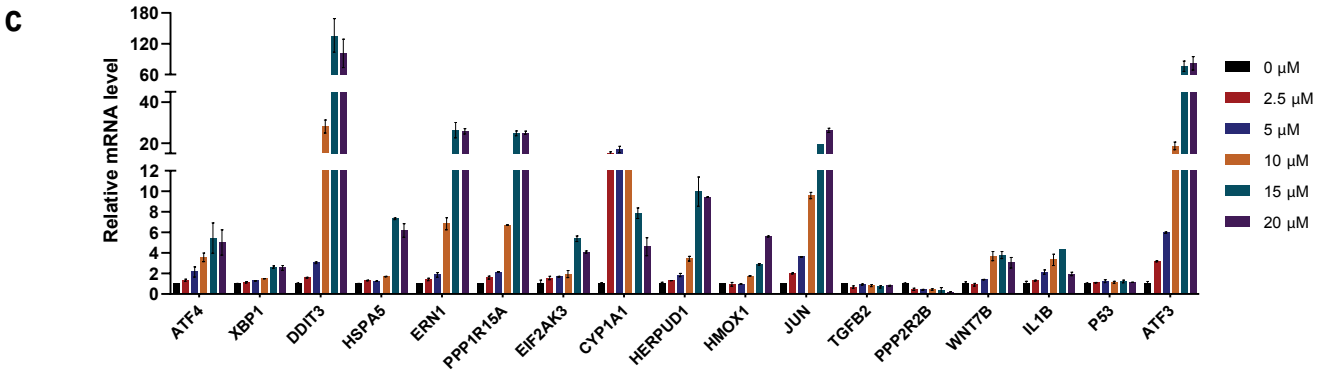

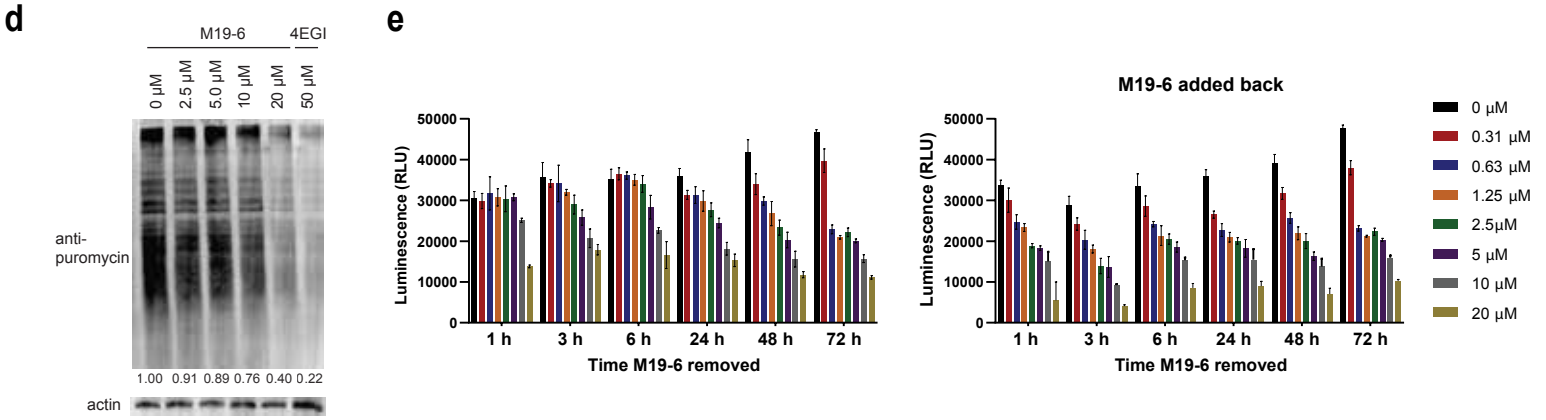

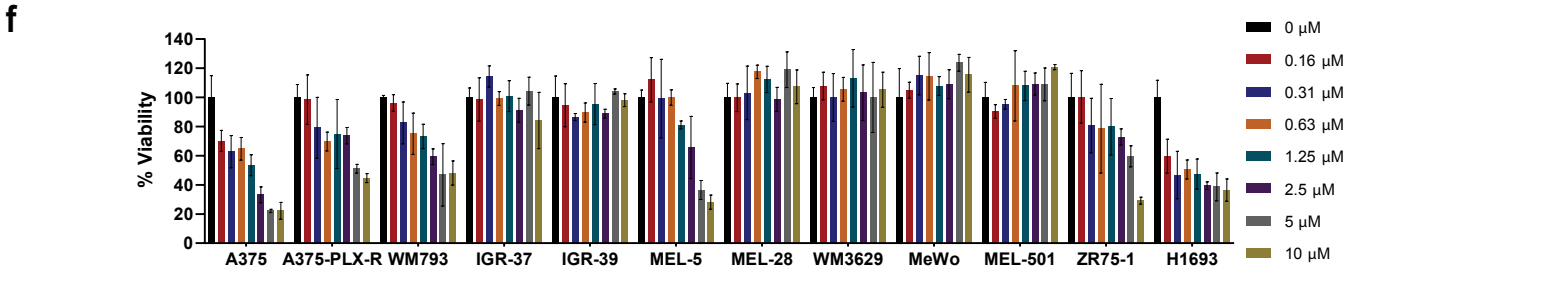

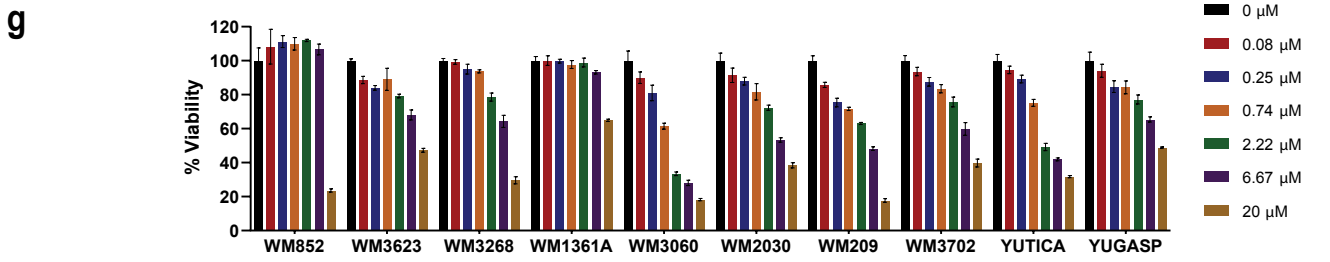

Feng Olea et al. Supp Fig. 4

H

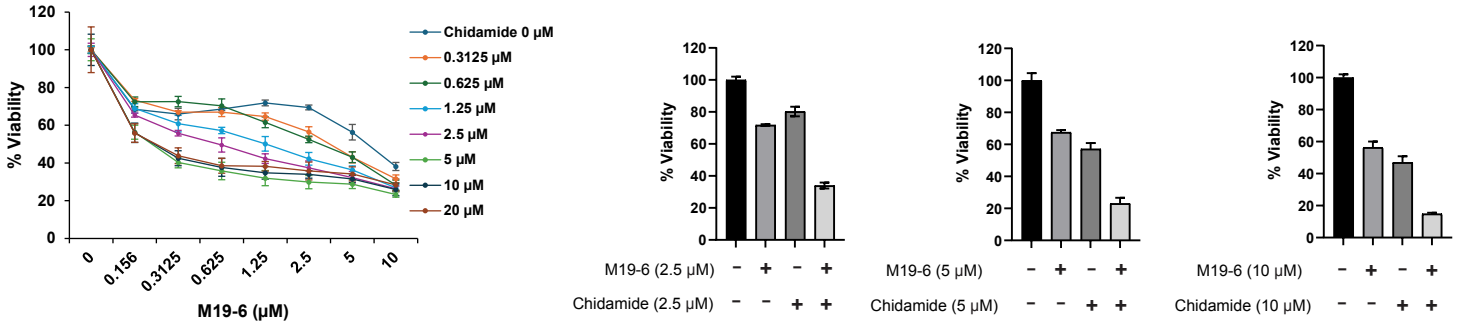
% Viability
M19-6 (μM)
0
0.156
0.3125
0.625
1.25
2.5
5
10
Chidamide 0 μM
0.3125 μM
0.625 μM
1.25 μM
2.5 μM
5 μM
10 μM
20 μM
M19-6 (2.5 μM)
Chidamide (2.5 μM)
M19-6 (5 μM)
Chidamide (5 μM)
M19-6 (10 μM)
Chidamide (10 μM)

I

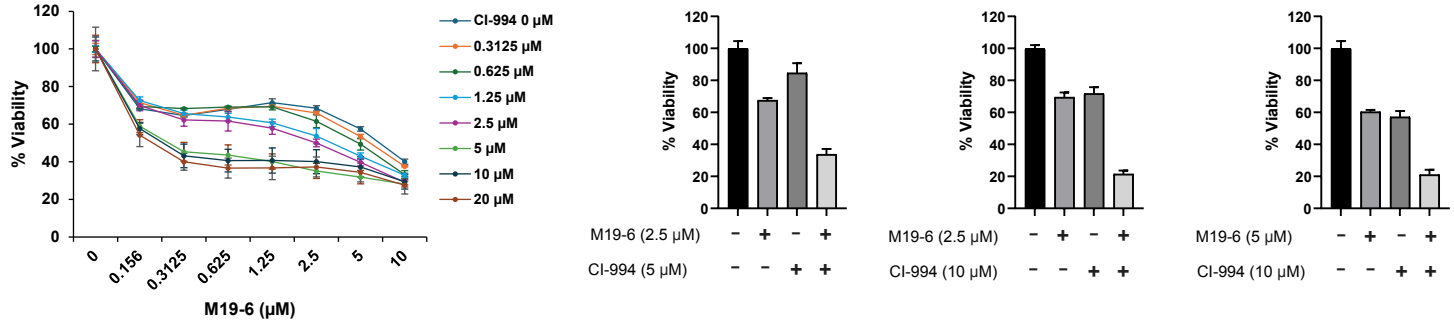
% Viability
M19-6 (μM)
0
0.156
0.3125
0.625
1.25
2.5
5
10
CI-994 0 μM
0.3125 μM
0.625 μM
1.25 μM
2.5 μM
5 μM
10 μM
20 μM
M19-6 (2.5 μM)
CI-994 (5 μM)
M19-6 (2.5 μM)
CI-994 (10 μM)
M19-6 (5 μM)
CI-994 (10 μM)

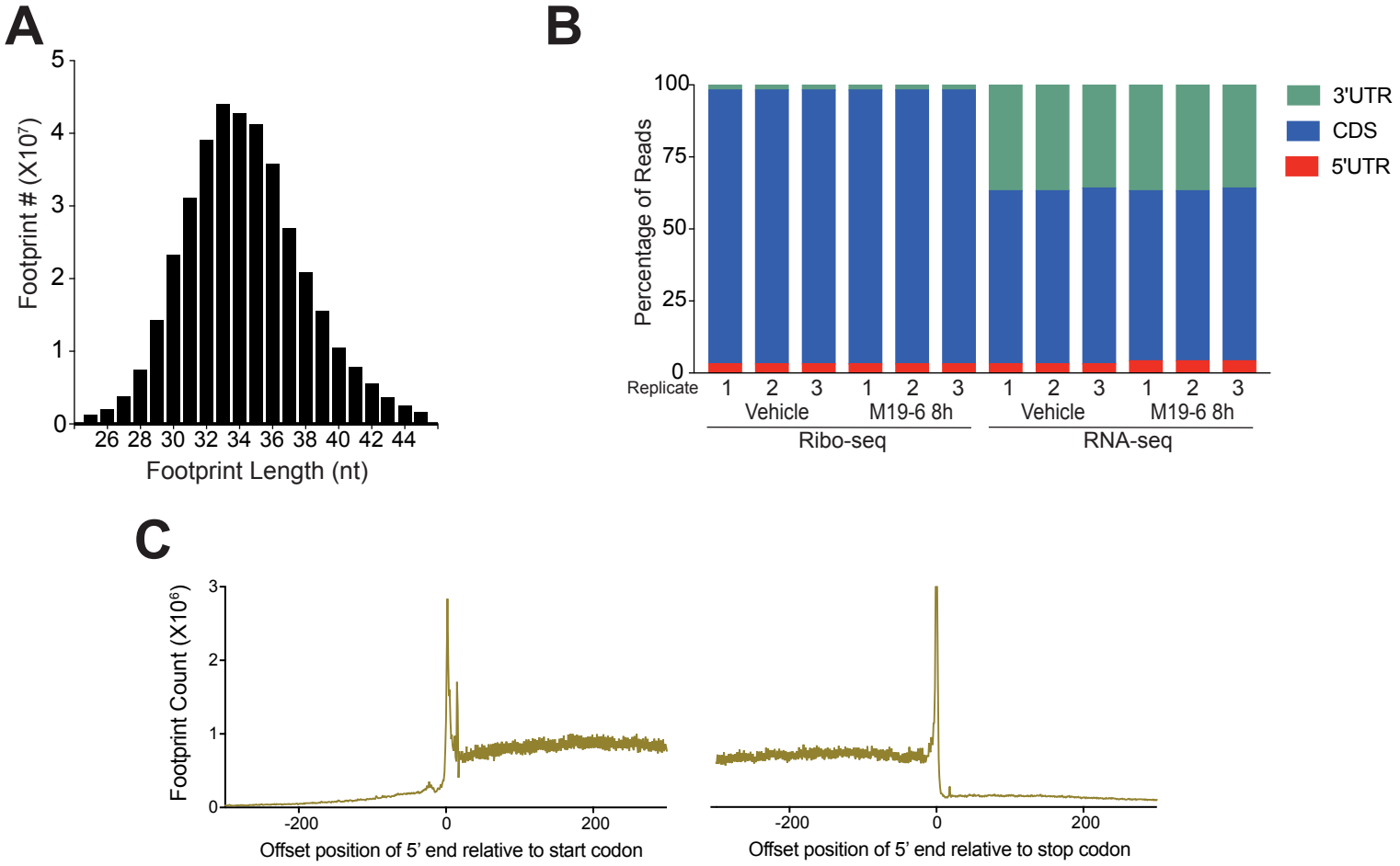

Feng, Olea et al., Supplementary Figure 5

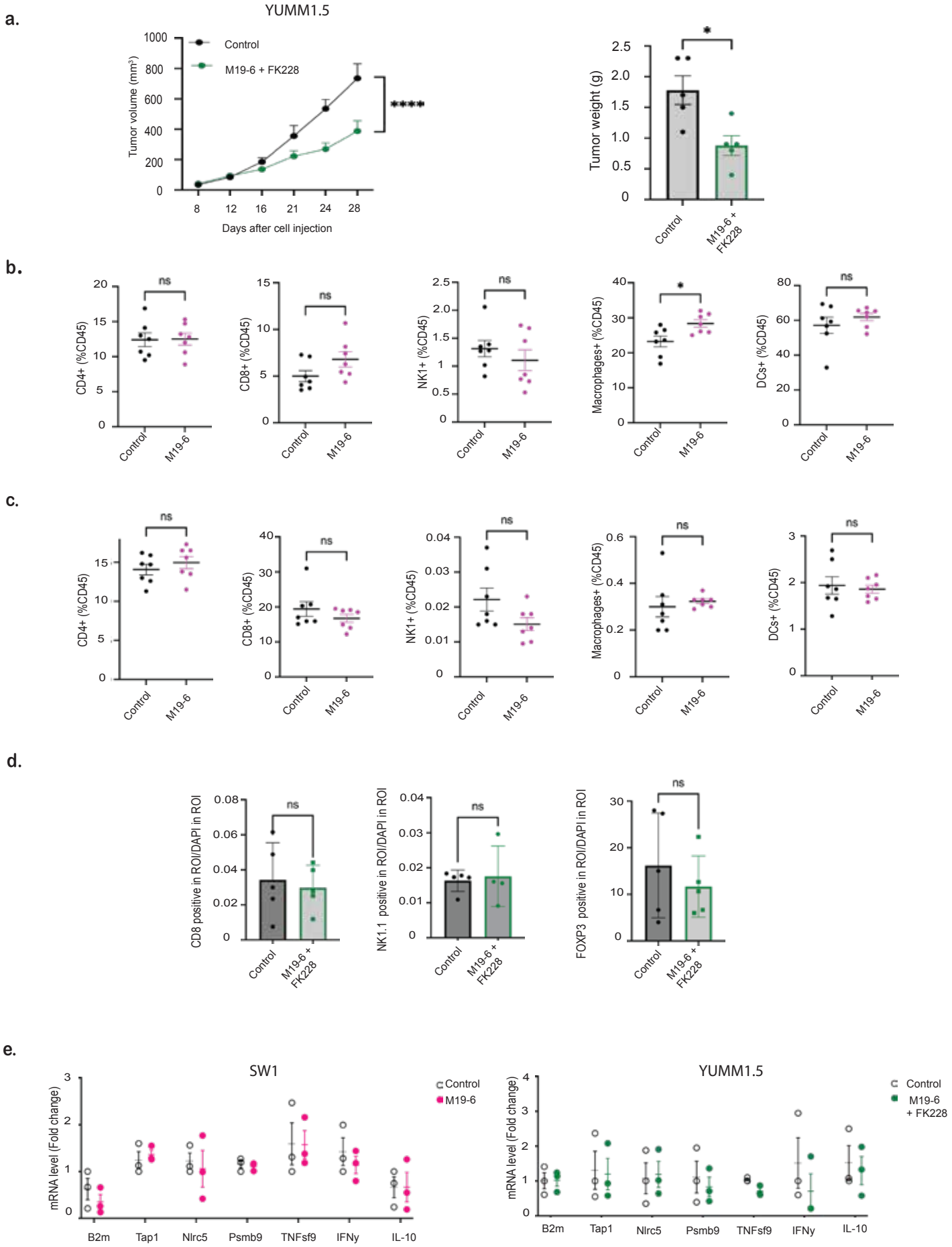

Feng Olea et al., Supp Fig 6